Inter-species h-current differences influence resonant properties in a novel human cortical layer 5 neuron model

Scott Rich[1,†], **Homeira Moradi Chameh**[1,†], **Vladislav Sekulic**[1,§], **Frances K. Skinner**[1,2,‡], **Taufik A. Valiante**[1,3,4,5,6‡]

***For correspondence:** sbrich@umich.edu (SR)

[†]Shared first authors
[‡]Shared senior authors

Present address: [§]RIKEN, Japan

[1]Division of Clinical and Computational Neuroscience, Krembil Research Institute, University Health Network (UHN), Toronto, Ontario, Canada; [2]Departments of Medicine (Neurology) and Physiology, University of Toronto, Toronto, ON, Canada; [3]Institute of Biomaterials and Biomedical Engineering, University of Toronto, Toronto, ON, Canada; [4]Institute of Medical Science, University of Toronto, Toronto, ON, Canada; [5]Division of Neurosurgery, Department of Surgery, University of Toronto, Toronto, ON, Canada; [6]Electrical and Computer Engineering, University of Toronto, Toronto, ON, Canada

Abstract

Most existing multi-compartment, mammalian neuron models are built from rodent data. However, our increasing knowledge of differences between human and rodent neurons suggests that, to understand the cellular basis of human brain function, we should build models from human data. Here, we present the first full spiking, multi-compartment model of a human layer 5 cortical pyramidal neuron. Model development balanced prioritizing current clamp data from the neuron providing the model's morphology, while also ensuring the model's generalizability via preservation of spiking properties observed in a secondary population of neurons, by "cycling" between these data sets. The model was successfully validated against electrophysiological data not used in model development, including experimentally observed subthreshold resonance characteristics. Our model highlights kinetic differences in the h-current across species, with the unique relationship between the model and experimental data allowing for a detailed investigation of the relationship between the h-current and subthreshold resonance.

Introduction

Currently, much of what is understood about specific cell-types and their role in "computation" (***Womelsdorf et al., 2014***) within the six-layered neocortex stems from invasive and *in vitro* studies in rodents and non-human primates. Whether or not such principles can be extended to human neocortex remains speculative at best. Despite the significant transcriptomic convergence of human and mouse neurons (***Hodge et al., 2019***), significant differences between human and rodent cell-type properties exist. *In vitro* studies have identified differences between mouse and human neurons in morphology (***Mohan et al., 2015***), dendritic integration (***Beaulieu-Laroche et al., 2018***; ***Eyal et al., 2016***), synaptic properties (***Verhoog et al., 2013***), and collective dynamics (***McGinn and Valiante, 2014***; ***Molnár et al., 2008***; ***Florez et al., 2013***). However, less explored are the active

membrane properties of human cortical neurons, which together with their passive and synaptic properties underlie oscillations which are of likely physiological relevance (***Akam and Kullmann, 2014***; ***Womelsdorf et al., 2014***; ***Fries, 2005***; ***Anastassiou et al., 2011***; ***Hanslmayr et al., 2019***; ***Vaz et al., 2019***).

Recently it has been shown that increased expression of hyperpolarization activated cation channels (h-channels) contribute to the observed subthreshold resonance in supragranular layer human pyramidal cells not seen in their rodent counterparts (***Kalmbach et al., 2018***). Such differential expression of h-channels also appears to be present between superficial and deep layer neurons of human cortex, with layer 5 (L5) pyramidal cells demonstrating a larger sag voltage mediated by the current through these channels (dubbed the "h-current") when compared to those in layer 2/3 (L2/3) (***Chameh et al., 2019***). However, despite the presence of large sag currents in human L5 pyramidal cells, they do not display subthreshold resonance (***Chameh et al., 2019***), a surprising result based upon recent human work (***Kalmbach et al., 2018***) as well as findings that rodent L5 pyramidal cells exhibit subthreshold resonance (***Silva et al., 1991***; ***Ulrich, 2002***; ***Dembrow et al., 2010***; ***Schmidt et al., 2016***).

To explore this seeming inconsistency, a combination of computational and experimental techniques are employed to create a novel human neuron model with a particular focus on the h-current. The development of computational models of human neurons with high levels of biophysical detail are more challenging than their rodent counterparts due to limited access to tissue for experimental recordings. This challenge is exacerbated by the fact that to model how a specific channel contributes to cellular dynamics, it is typically necessary to obtain a complete data set (including whole-cell recordings in current and voltage clamp modes, pharmacological manipulations, and 3D morphology) all in the same neuron. The increased access to rodent tissue makes accounting for these concerns more feasible in the rodent setting, and explains why a majority of the existing biophysically detailed neuron models are constrained by rodent data (***Dong, 2008***; ***Jones et al., 2009***; ***Sunkin et al., 2012***). Nonetheless, the clear differences between human and rodent neurons (***Hodge et al., 2019***; ***Eyal et al., 2018***, ***2016***; ***Testa-Silva et al., 2014***; ***Verhoog et al., 2013***; ***Beaulieu-Laroche et al., 2018***) leads to two important questions for computational neuroscientists: in what settings is it appropriate to utilize rodent neuron models to glean insights into the human brain, and when such approximations are undermined by inter-species differences, can the functional role of these differences be identified?

We address these questions via a modeling framework that makes use of a detailed data set obtained from a single human L5 neuron. We are motivated by the clear preponderance of the h-current in human L5 neurons (***Chameh et al., 2019***), their complex role in regulating neuronal excitability (***Dyhrfjeld-Johnsen et al., 2009***; ***Biel et al., 2009***), their hypothesized role in driving subthreshold resonance (***Kalmbach et al., 2018***; ***Hu et al., 2002***, ***2009***; ***Zemankovics et al., 2010***; ***Ulrich, 2002***), and towards developing human inspired neuronal models for brain simulators (***Einevoll et al., 2019***).

Since it is clear that the characteristics of a given cell type are not fixed (***Marder and Goaillard, 2006***), and moreover that this inherent variability amongst similarly classified cells could be functionally important (***Wilson, 2010***), we develop a modeling approach that directly accounts for the challenge posed to modelers by such "cell-to-cell variability". Our "cycling" model development strategy primarily constrains the model using current clamp data and morphology from the same neuron. In a second step, we ensure the model retains spiking characteristics exhibited by a population of secondary human cortical L5 pyramidal neurons; the process cycles between these two steps to obtain an optimal model. The resulting multi-compartment, fully spiking human L5 neuron model recapitulates the electrophysiological data from hyperpolarizing current clamp experiments in the primary cell remarkably well, while also demonstrating repetitive and post-inhibitory rebound spiking properties characteristic of human L5 pyramidal cells from the secondary data set (***Chameh et al., 2019***).

A key aspect of our approach was to "fit" the h-current kinetics to the current clamp data,

which was then validated by comparing the kinetics of our current clamp derived "human" h-current model to experimentally-derived kinetics from voltage clamp data not used as a modeling constraint. These kinetics are distinct from those observed in rodents and implemented in many rodent cortical pyramidal cell models (***Kole et al., 2006***). With the model validated, a detailed investigation into the generation of subthreshold resonance in these cells reveals that the unique kinetics of the human h-current we describe here explain the lack of resonance seen in human L5 pyramidal cells (and replicated by our model) despite the abundance of these channels (***Chameh et al., 2019***). Taken together, our model predictions are validated against data from the primary neuron not used in model generation, as well as against data from a larger cohort of many additional human L5 cortical pyramidal cells (***Chameh et al., 2019***), including complex subthreshold dynamics exemplified by the lack of resonance.

In summary, our findings reveal that there are important differences in dynamics of the h-current in human L5 pyramidal neurons, when compared to their rodent counterparts, that obviate subthreshold resonance at resting membrane potential despite the presence of large sag currents. Given the numerous ways in which the validity of the model used in this investigation are confirmed, this technique is likely more generally applicable to other modeling endeavors. Critically, this publicly available cell model represents the first biophysically detailed, multi-compartment human L5 pyramidal model with active dendrites that can be used and modified to investigate distinctly human neural dynamics.

Results

Development of a human L5 cortical pyramidal cell model using a cycling fitting strategy

In developing models of a given cell type it is preferable to use data from the same cell, as averaging experimental data from multiple cells in order to create computational models has been shown to be problematic due to cell-to-cell variability (***Golowasch et al., 2002***). Indeed, multiple studies have shown significant variability in conductance densities between similarly classified neurons (***Goaillard et al., 2009***; ***Ransdell et al., 2013***). However, obtaining the full suite of data necessary to completely characterize all the different ion channel types individually is not possible in an individual neuron given experimental constraints (a discussion of these limitations is included in the Materials and Methods). This is additionally challenging when building human cellular models due to limited tissue access.

Given these considerations, we developed a "cycling" fitting methodology (inspired in part by the "divide and conquer" strategy proposed by ***Roth and Bahl*** (***2009***)) to best utilize our unique human data set to build our model. Two distinct sets of data were utilized: data from our primary neuron, from which detailed morphology and electrophysiological recordings in the presence of tetrodotoxin (TTX, which blocks voltage-gated sodium channels and in turn action potential generation) were obtained, shown in Figure 1; and data from a suite of secondary neurons, not treated with TTX, that yielded spiking characteristics (***Chameh et al., 2019***).

Our model generation process began with a reconstruction of the primary neuron's cellular morphology, illustrated in Figure 1, and implementation of this reconstruction in the NEURON simulation environment (***Carnevale and Hines, 2006***). In the absence of any other specific knowledge of the human setting, we included ten different types of ion channels that were used in developing rodent L5 pyramidal cell models (***Hay et al., 2011***). They include the following: a fast, inactivating sodium current (abbreviated Na_Ta); a persistent sodium current (abbreviated Nap_Et2); a slow, inactivating potassium current (abbreviated K_Pst); a fast, non-inactivating potassium current (abbreviated SKv3_1); a small-conductance calcium activated potassium current (abbreviated SK_E2); a fast, inactivating potassium current (abbreviated K_Tst); a low-voltage activated calcium current (abbreviated Ca_LVA); a high-voltage activated calcium current (abbreviated Ca_HVA); the non-specific hyperpolarization-activated cation current (abbreviated Ih); and the voltage-gated mus-

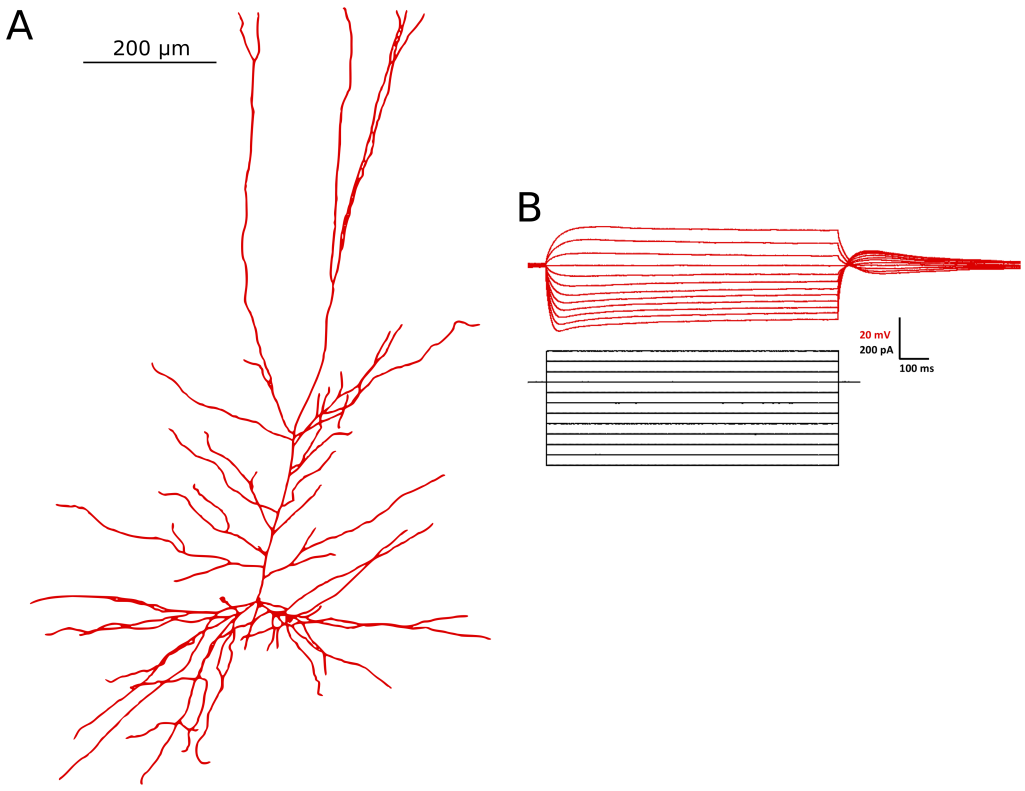

Figure 1. Morphology and current clamp data obtained from the primary neuron. **(A)** The morphology of the primary neuron was reconstructed using IMARIS software and imported into NEURON (which generated the plot shown here). **(B)** Current clamp recordings from the primary neuron in the presence of TTX that are the primary constraining data for model development.

carinic potassium channel (abbreviated Im). Note that the abbreviations used here are motivated by the labeling used in the NEURON code for consistency. This provided the initial basis for our model construction, with further details included in the Materials and Methods.

The "cycling" technique schematized in Figure 2 built upon this basis. In the first step, an optimization algorithm was run to best "fit" the model's output with blocked sodium channels to experimental data from current clamp recordings in the presence of TTX (see Figure 1). This determined a majority of the conductances used in the model, as well as the passive properties and the kinetics of the h-current. As the h-current is the primarily active inward current at hyperpolarized voltages (***Toledo-Rodriguez et al., 2004***; ***Hay et al., 2011***), we focused on it by emphasizing hyperpolarizing current clamp traces in our fitting and by optimizing both the conductance and kinetics of this channel type.

In the second step, after a best fit was achieved, we hand tuned the conductances involved in action potential firing (sodium conductances and the K_Pst and SKv3_1 potassium conductances, which were not altered in the preceding step), along with minor alterations to the dynamics of these channels (see details in the Materials and Methods). The goal of this step was to ensure the spiking behavior of our model cell was reasonable in comparison to the range of spiking properties, both of repetitive and post-inhibitory rebound (PIR) firing, exhibited by secondary human L5 pyramidal cells (summarized in Table 1 (***Chameh et al., 2019***)). We aimed to obtain these firing characteristics with minimal potassium conductances, in order to minimize the error seen in Figure 3**E**: an extensive exploration of the parameter space revealed that a "best fit" of this trace would enforce values of the potassium conductances that would not permit action potential firing, motivating the hand tuning of these values in search of a set of sodium and potassium conductance values that would permit spiking while also minimizing this error. As the properties of these potassium channels

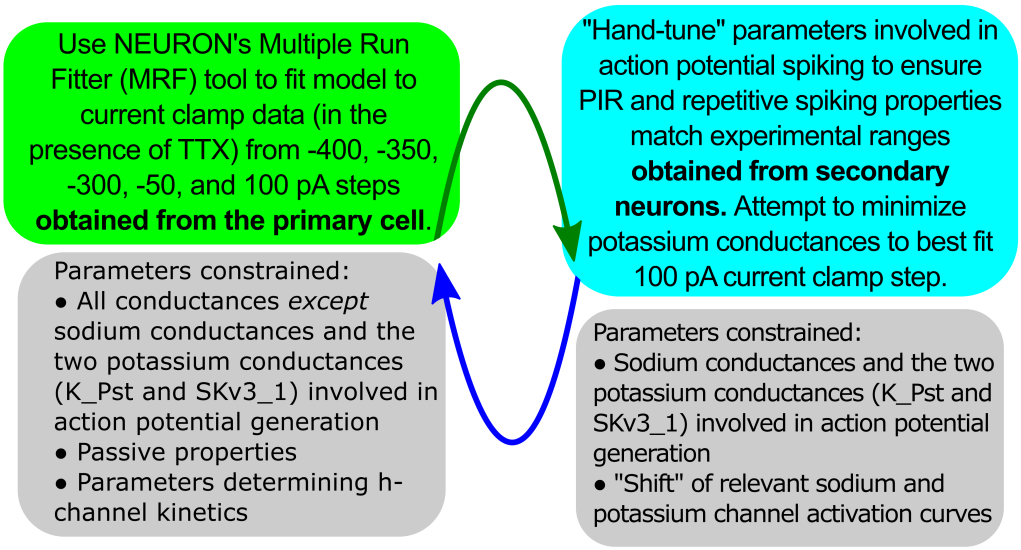

Figure 2. Diagram of the model development strategy. Hyperpolarizing current clamp data taken from the primary human L5 pyramidal cell was the primary constraint in determining model parameters. To ensure that the model exhibited repetitive and post-inhibitory rebound firing dynamics characteristic of human L5 pyramidal cells, data from secondary neurons, as well as best fit data from depolarizing current clamp experiments in the primary cell were used, and a "cycling" technique was developed in which conductances primarily active during spiking dynamics were fit separately by hand. The adjustments to the potassium conductances affect the current clamp fits, so these were re-run with the new values, hence the "cycle".

affected the current clamp fits, it was then necessary to run the optimization algorithm of the first step again with these new values, hence the "cycling". This cycling pattern continued until no further improvement in the model, as determined via the quantitative error score from the optimization process as well as the more qualitative matching of spiking properties, could be obtained (see the Materials and Methods for further details).

Table 1. Properties of repetitive and post-inhibitory rebound (PIR) spiking observed experimentally in secondary population of human L5 pyramidal neurons compared to the model

	Mean ± STD Experimental	**Maximum Experimental**	**Minimum Experimental**	**Model**
Spiking Rate (Hz) 50 pA current step	2.5 ± 1.6	5.0	1.6	17.9
Spiking Rate (Hz) 100 pA current step	7.5 ± 8.3	45.0	1.7	37.0
Spiking Rate (Hz) 300 pA current step	63.3 ± 51.9	211.7	11.7	71.4
PIR Spike Latency (ms) -400 pA current step	95 ± 70	250	5.1	75
PIR Spike Latency (ms) -350 pA current step	85 ± 60	230	5.4	87
PIR Spike Latency (ms) -300 pA current step	96 ± 70	250	5.7	110

The output of our final model in response to the various current clamp protocols with blocked sodium channels, compared to what was observed experimentally in the primary neuron, is shown in Figure 3**A-E**. The repetitive spiking behavior of the model in response to various driving currents is shown in Figure 4**A-C**, and the capacity for PIR spiking is shown in Figure 4**D**; both of these protocols

are performed with active sodium channels. The repetitive firing frequency or latency to the first PIR spike (depending upon whether the protocol is a depolarizing or hyperpolarizing current clamp, respectively), is given in Table 1. Critically, the model closely matches all of the hyperpolarizing current clamp data, indicating that the dynamics of the h-current within this voltage range were accurately encapsulated by our model. While the error in the depolarizing current clamp recording (Figure 3**E**) is more noticeable, this was minimized via the process described above, and was the best case while also ensuring reasonable repetitive spiking and PIR spiking behaviors (Figure 4 and Table 1).

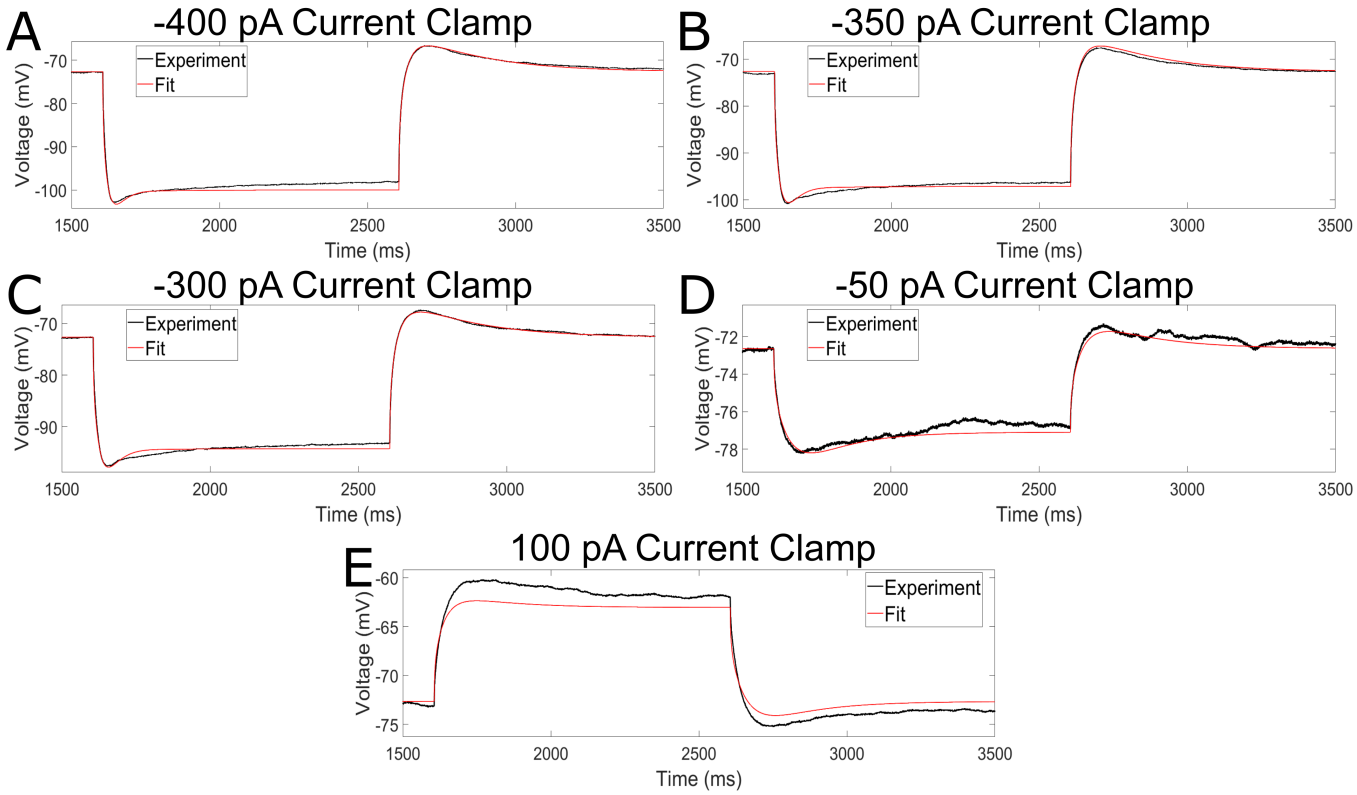

Figure 3. Model well fits data from hyperpolarizing current steps, in which the h-current is the primary active channel, while minimizing the error seen in a depolarizing current step. **(A-D)** Fits of current clamp data with -400 pA **(A)**, -350 pA **(B)**, -300 pA **(C)** and -50 pA **(D)** current steps with TTX. **(E)** Fit of current clamp data with a depolarizing current step of 100 pA with TTX. All four hyperpolarized current steps are fit with great accuracy, with a focus on the initial "sag" and post-inhibitory "rebound" that are driven by the activity of the h-current. While the charging and discharging portion of the depolarizing current trace is well fit, the amplitude of the response is less accurate; however, this error was deemed reasonable given the emphasis in model development on capturing h-current dynamics, including PIR spiking, as discussed in detail in the text.

Indeed, the repetitive spiking frequencies and latencies to the first PIR spike highlighted in Table 1 all fall within the range exhibited by the experimental data (see the maximum and minimum experimental values in Table 1), with the exception being the 50 pA current input resulting in faster spiking in our model than seen experimentally. This is likely a side effect of the "shift" in the sodium activation curves that, along with matching h-current features, was necessary to elicit PIR spiking in the model (described in detail in the Materials and Methods). Matching PIR behavior was deemed critical in this modeling endeavor given that the h-current is implicated in dictating this behavior (***Chameh et al., 2019***). Indeed, the areas in which the model does not match the experimental data with the same level of accuracy as elsewhere are reasonable given the focus of the model on h-current driven dynamics, which are observed primarily in the fit to the hyperpolarizing current steps and the ability of the model to exhibit PIR spiking.

Our assertion that this model is appropriate for use in settings beyond those directly constraining

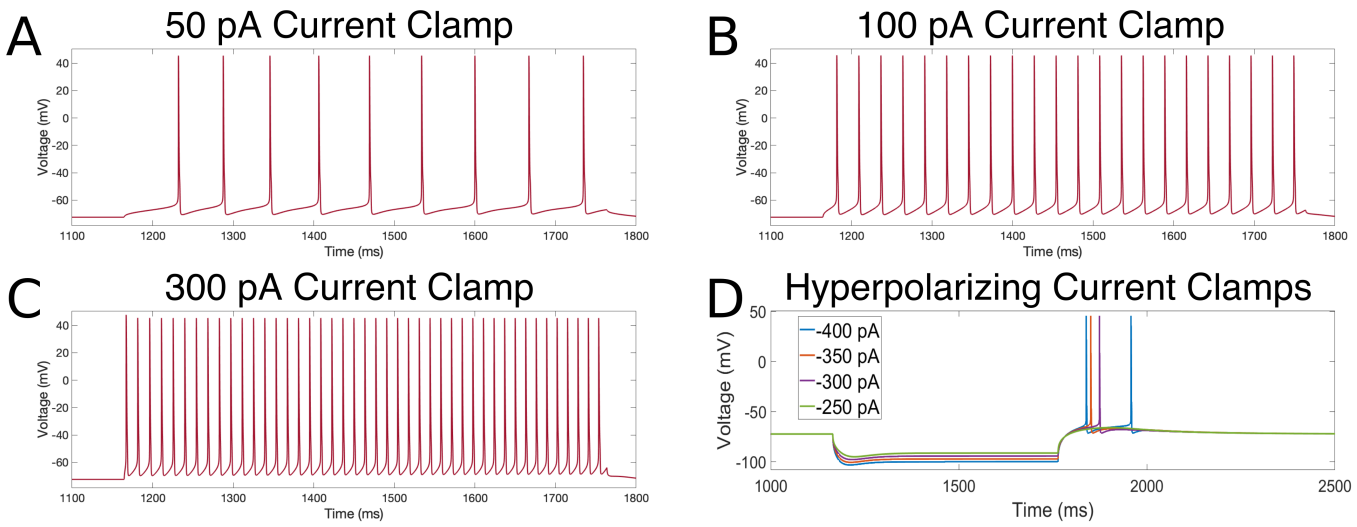

Figure 4. Model neuron exhibits reasonable repetitive and PIR spiking behavior. **(A-C)** Repetitive spiking behavior of the model neuron in response to a 50 pA **(A)**, 100 pA **(B)**, and 300 pA **(C)** current clamp steps. **(D)** PIR behavior in response to four hyperpolarizing current injections..

model generation requires additional evidence. Indeed, we must rule out the possibilities that we accidentally "overfit" our model to the chosen constraining data, or that this chosen data was somehow idiosyncratic and not indicative of the general properties and dynamics of the primary neuron and human L5 cortical pyramidal cells generally. We accomplish this task in three ways: first, by testing the model against secondary current clamp data obtained from the primary neuron but not used in model development (below); second, by comparing the dynamics of the modeled human h-current to those observed experimentally in the primary neuron (in the following section); and third, by comparing the model's capacity for subthreshold resonance with that observed experimentally in human L5 cortical pyramidal neurons generally (in the following section).

Figure 5 illustrates the output of the model with four hyperpolarizing current injections, in comparison to the experimentally observed output from primary cell, that were not directly "fit" in model generation. We again focus on hyperpolarizing current steps given the focus on the h-current, which is activated at hyperpolarized voltages, in this endeavor. The strong correspondence between the model and the experimental data illustrates that the modeling process described here does indeed capture the general behavior of the primary cell in response to hyperpolarizing current steps of varying amplitudes. Perhaps most importantly, in all four cases the features of the trace most prominently influenced by the h-current, the initial "sag" following the onset of the hyperpolarizing current step and the "rebound" following its release, remain reasonably approximated by the model.

This result is a straightforward way of assessing our model's validity via its ability to well match additional current clamp traces from the primary cell. Furthermore, considering the h-current's dominance over the neuron's dynamics at these hyperpolarized voltages, this result also provides early support for our assertion that our model captures the dynamics of the h-current. We more directly validate this assertion via the kinetics of the h-current and one important functional implication of these kinetics, subthreshold resonance, in the following section.

Model replicates h-current kinetics and subthreshold resonance features observed experimentally

The distinct kinetics of the human h-current model from those of the rodent model of ***Kole et al.*** (***2006***) were paramount in facilitating the accurate fits of the *in silico* model (see Figure 3) to the *in vitro* experimental data presented in Figure 1. Such dynamics were constrained solely via the optimization technique summarized above. With these fits in hand alongside the presence of additional experimental data, namely voltage clamp recordings from both the primary neuron and

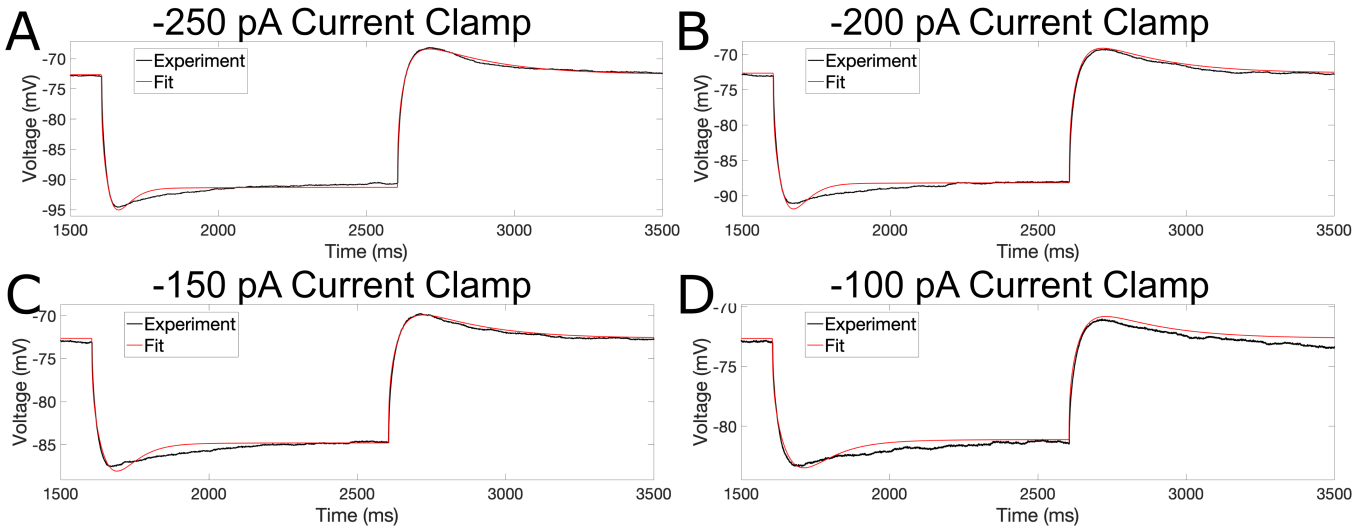

Figure 5. Model output well-matches experimental data not used as constraints in model generation. **(A-D)** Voltage traces from current clamp experiments with blocked voltage-gated sodium channels for steps of -250 pA **(A)**, -200 pA **(B)**, -150 pA **(C)** and -100 pA **(D)**. Model output (red curve) well matches the experimental observations (black curve) despite these traces not being used in model generation.

secondary human L5 cortical pyramidal cells (described in detail in the Materials and Methods), approximate experimental values of the voltage dependence of the time constant (denoted τ) and the steady-state activation values of the h-current are obtained and compared with the h-current model derived from our modeling process.

In Figure 6 we present a comparison of the experimental values of these quantities, alongside the human h-current model as well as the model of ***Kole et al.*** (***2006***) that was used by ***Hay et al.*** (***2011***). Given space-clamp issues associated with voltage clamp recordings, along with the fact that these recordings are somatic and h-channels are distributed throughout the dendrites both biologically and in our model, we would not expect our model to perfectly match this experimental data. However, it is apparent that our human h-current model is a better approximation of the experimental data, in particular that associated with the primary neuron, than the rodent h-current model. This is especially apparent for the voltage dependence of the time constant. We emphasize that the experimental voltage clamp data is *only* used for model validation, *not* for model creation, in order to maintain a self-consistent modeling strategy (a choice that is elaborated on in the Materials and Methods).

We note that, based upon the current clamp data for which the human h-current model parameters were derived, it would be expected that the best fit to the experimentally observed kinetics obtained from the voltage clamp data would be in a voltage range of -90 to -60 mV (which notably includes the cell's resting membrane potential), as this is the range at which a majority of the constraining current clamp data lies: because the current clamp data never achieves extreme hyperpolarized values (i.e. well past -100 mV), there is minimal constraint on the model at these voltages. This serves to explain why the τ values of the human h-current approach zero much quicker for voltages in this hyperpolarized regime than indicated by the voltage clamp derived data (and, given the continuity of the modeled τ function, why this influence expands into the more hyperpolarized values of even our "best constrained" voltage range). An approximate range of voltages for which the human h-current model is best constrained, and thus most reasonably expected to be validated by this secondary experimental data, is highlighted in Figure 6 and "zoomed in" on in the second and fourth rows.

There are clear correspondences between the human h-current model's kinetics and those derived from voltage clamp protocols that highlight differences between the human and rodent kinetics, especially when the model presented here is compared to the rodent model of ***Kole et al.***

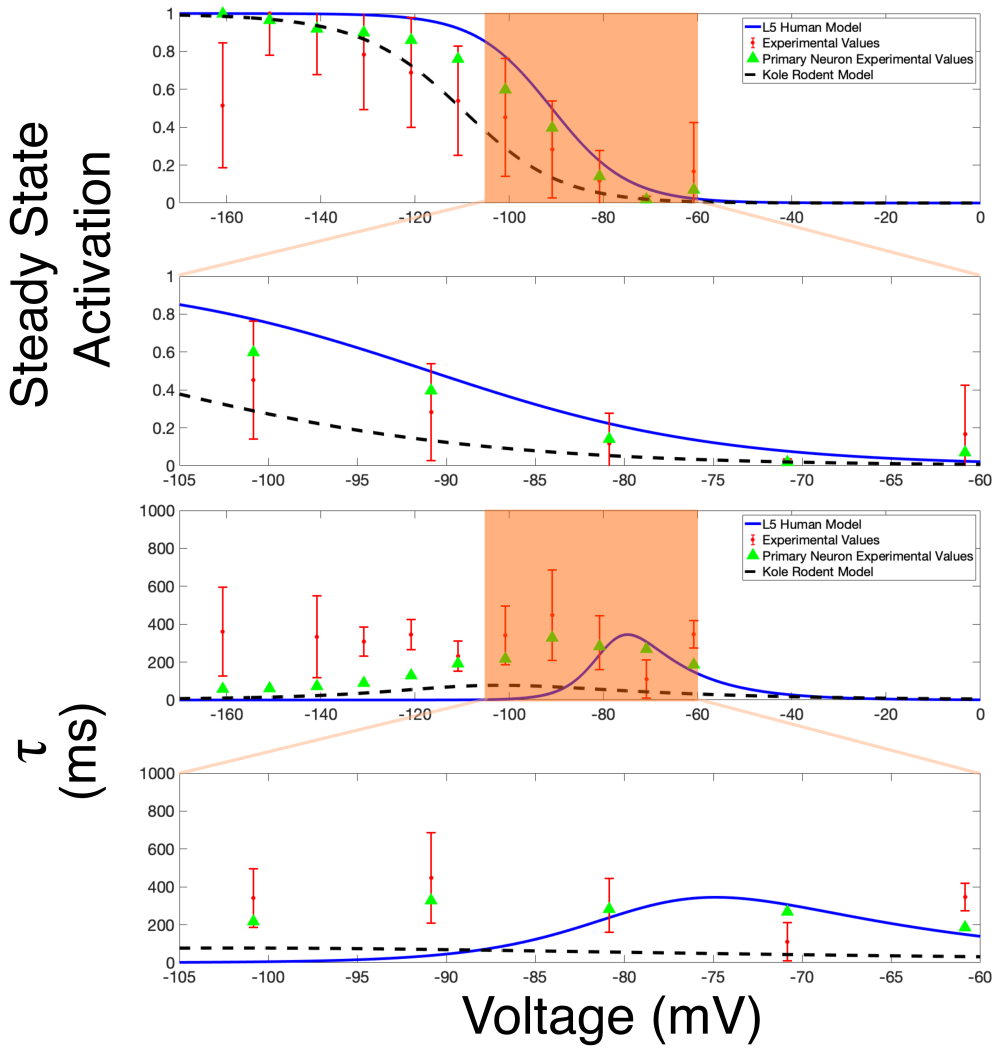

Figure 6. The human h-current model presented in this work is validated by comparison to experimental voltage clamp data. Plots of steady-state activation (top two rows) and τ (bottom two rows) curves, where the entire voltage range is shown on top, with the voltage range where the model is primarily constrained highlighted in orange and then displayed "zoomed in" below. The values for our L5 human h-current model are shown in blue, with these values juxtaposed with those extracted from voltage clamp experiments: data from the primary cell are shown via green triangles, and data averaged over a number of L5 cortical pyramidal cells (with the standard deviation shown via error bars) are shown in red. For comparison, analogous curves from the ***Kole et al.*** (***2006***) rodent h-current model are shown via a dotted black line.

(***2006***). We note that these differences are also apparent in the experimental data alone, but we focus on the differences in the models given the aims of this study. Most importantly, the human experimental data shows maximum τ values around 400-500 ms. The maximum τ value in the human h-current model is similar, at approximately 350 ms. However, the ***Kole et al.*** (***2006***) model is different by an order of magnitude, never exceeding 80 ms. The experimental data shows that the τ value of the human h-current should be significantly higher than that typically seen in rodents, a feature replicated by our model.

Our human h-current model matches the kinetics predicted by the voltage clamp experiments, particularly those from the same cell, very well within the voltage range at which the data was most constrained. The τ values between -80 to -60 mV are a close fit with the human h-current model, whereas those of the ***Kole et al.*** (***2006***) model are off by approximately an order of magnitude. Moreover, the steady state activation curve fits the experimentally observed values in the primary

neuron very well between -100 and -80 mV, and qualitatively better matches the "shape" of the primary neuron's values than the ***Kole et al.*** (***2006***) model.

Taken together, these pieces of data validate that our human h-current model is biologically reasonable based on the available experimental results, particularly those from the primary neuron. Critically, the relative magnitude of the τ values in our model and the ***Kole et al.*** (***2006***) model lend support to the viability of our model in human L5 neurons.

The accuracy of the h-current kinetics predicted by our model is pivotal, and justifies our model development approach generally. The fact that we can use mathematical modeling to accurately describe the unique characteristics of the h-current in this setting indicates that the cycling technique described here could be successfully applied to other modeling endeavors where experimental data from a single cell is similarly limited. In the specific context of this work, these different kinetics and their validation allow for a comparison between rodent and human h-current kinetics. Moreover, considering that the h-current is implicated throughout the literature in determining subthreshold resonance (***Kispersky et al., 2012***; ***Zemankovics et al., 2010***; ***Hu et al., 2002***; ***Kalmbach et al., 2018***), this model now provides an opportunity to probe the relationship between this particular ionic current and this neural dynamic.

We first investigate the model's capacity for subthreshold resonance by recording the voltage response to the application of a subthreshold ZAP current. We focus on this protocol because data describing the response of human L5 cortical pyramidal cells to this experimental paradigm *in vitro* are presented by ***Chameh et al.*** (***2019***) and so allow comparison. In particular, the human L5 cortical pyramidal cells studied in that work do not exhibit subthreshold resonance. When analogous *in silico* protocols to the experiments presented by ***Chameh et al.*** (***2019***) are performed (described in detail in the Materials and Methods section), our model does not exhibit subthreshold resonance, as shown in Figure 7**A** (in comparison to experimental results shown in Figure 7**B**). We note that we will compare these results to those from rodent-derived models in the following section.

This finding provides further validation for our model: despite subthreshold resonance dynamics not being used to directly constrain our model, our model replicates what is seen experimentally under this protocol. This validation extends generally to our modeling approach, as this finding implies that features that were actively "fit" in model generation, in particular the condutances and passive properties dictating the voltage response to hyperpolarizing current clamp traces, are essential in driving other, more complex neural dynamics.

Taken together, these validation studies indicate that this model provides a means by which one could explore human-specific dynamics in L5 cortical pyramidal cells. Specifically, an investigation into the relationship between the detailed biophysical model and its various ionic currents (particularly the h-current) and subthreshold behaviours is now well justified. Indeed, the lack of subthreshold resonance observed experimentally by ***Chameh et al.*** (***2019***) was somewhat surprising, as subthreshold resonance (in the 3-5 Hz range) is observed in some superficial layer human pyramidal neurons (***Kalmbach et al., 2018***) and rodent L5 pyramidal neurons (***Silva et al., 1991***; ***Ulrich, 2002***; ***Dembrow et al., 2010***; ***Schmidt et al., 2016***). These experimental results also showed that the "sag" voltage indicating the presence of h-channels is more pronounced in human L5 cells as opposed to deep layer L2/3 (***Kalmbach et al., 2018***; ***Chameh et al., 2019***). Considering the consensus that the h-current play some role in driving subthreshold resonance (***Hu et al., 2002***, ***2009***; ***Zemankovics et al., 2010***; ***Kalmbach et al., 2018***), these findings might initially seem contradictory. Our model neuron is uniquely situated to probe this relationship in detail.

Inter-species h-current kinetic differences influence dichotomous subthreshold resonance characteristics in model neurons

With the model validated, we now compare the behavior of our human L5 cortical pyramidal cell model to two other existing models. The first model is the rodent L5 cortical pyramidal model as developed by ***Hay et al.*** (***2011***), which motivated the ion channel types implemented in the human model (see the Materials and Methods). The second model is the human deep L3 pyramidal cell

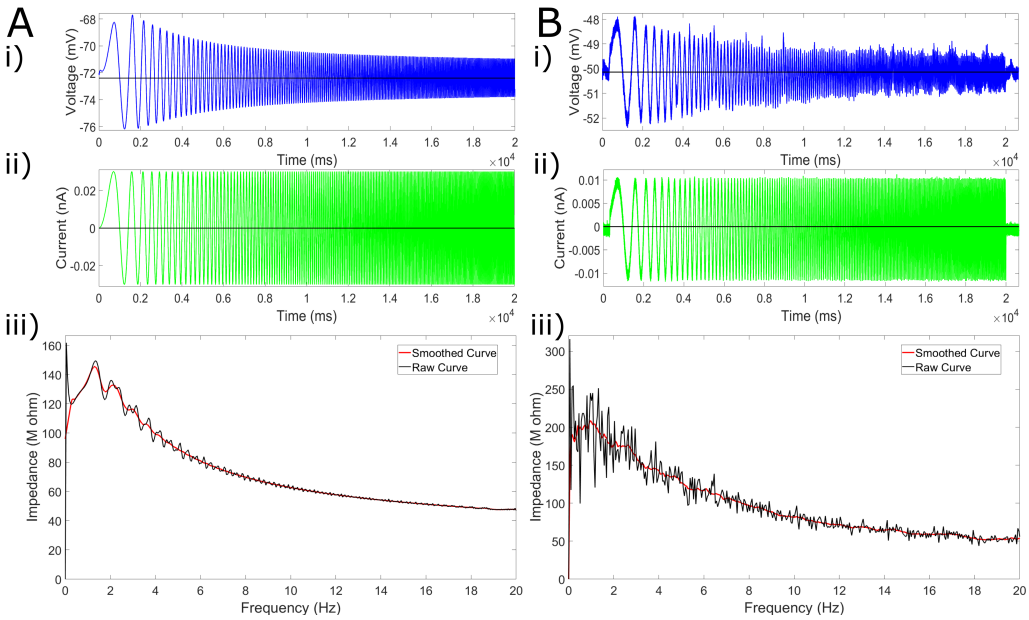

Figure 7. Model matches experimental data from human L5 pyramidal neurons lacking subthreshold theta resonance in response to ZAP function input. **(A)** *In silico* results from the model neuron to subthreshold current input from a ZAP function. The voltage response is shown in **i)**, the input current in **ii)**, and the calculated impedance in **iii)**, illustrating the lack of a peak at theta frequency. **(B)** Example *in vitro* results of an analogous ZAP protocol (plots correspond with those in panel **A**) show the lack of subthreshold resonance experimentally.

model of ***Kalmbach et al.*** (***2018***), which was built based on human deep L3 morphological and electrophysiological data with the h-channel as the only voltage-gated ion channel type present in the model (see the Materials and Methods for details).

The h-current models used in each of these three models are compared in Figure 8. Moving forward, we will refer to the cell model presented in this paper as the "L5 Human" model to differentiate it from the Hay and Kalmbach models. The dynamics of the h-current model in the L5 Human model is as shown previously in Figure 6 in comparison with experimental data. Figure 6 also included the rodent model of ***Kole et al.*** (***2006***) that is used by ***Hay et al.*** (***2011***). The differences between our human h-current model compared to the rodent Kole model are that the steady state activation curve is shifted significantly towards more positive voltages, and the kinetics are much slower (indicated by larger values of τ), between approximately -90 and -40 mV. In Figure 8, these differences can be seen and compared to the h-current model that is used by ***Kalmbach et al.*** (***2018***), which is a slight adaptation of the model presented by ***Kole et al.*** (***2006***) (described in detail in the Materials in Methods).

Given the impetus of this modeling endeavor, we compare the capacity for each of these three models to exhibit subthreshold resonance. In applying an identical ZAP protocol as above for our L5 Human model (see Figure 7), we find that both of these other models, unlike our L5 Human model, exhibit subthreshold resonance at approximately 4.6 Hz as shown in Figure 9.

A quantification of these model comparisons is given in Table 2. Alongside results for the baseline models (illustrated in Figure 9), we also include results for the L5 Human and Hay models with all channels besides the h-channel blocked in order to facilitate a more direct comparison with the Kalmbach model (which has no other active ion channels). This alteration results in a minor change in the resting membrane potential (RMP) of the neuron, as would be expected, but no major change in its resonance frequency.

The finding that the Hay model exhibits subthreshold resonance is as expected considering that subthreshold resonance has been previously observed in rodent L5 cortical pyramidal cells

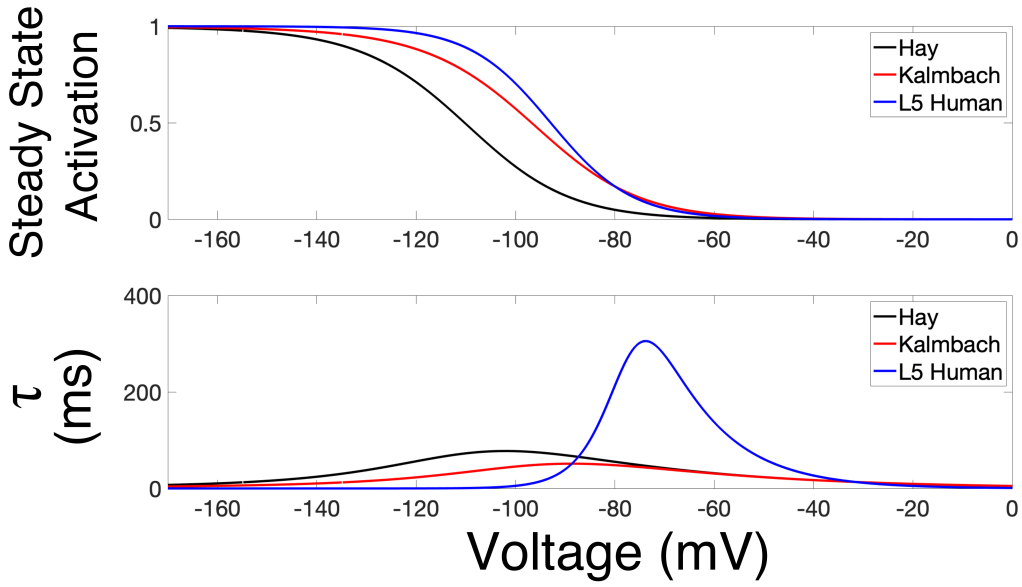

Figure 8. Comparison of h-current models used in three cortical pyramidal neuron models. Plot of steady-state activation curve (top) and τ (bottom) of the h-current model used by ***Hay et al.*** (***2011***), ***Kalmbach et al.*** (***2018***), and in the model presented in this paper (referred to as "L5 Human").

Table 2. Quantified results of the ZAP protocol applied to the three pyramidal cell models of interest highlight different propensities for subthreshold resonance.

Model	Conditions	RMP	Frequency of Peak Impedance (>1 Hz)
L5 Human	Default	-72.40 mV	1.35 Hz
L5 Human	Block all channels besides h-channel	-72.00 mV	1.37 Hz
Hay	Default	-77.25 mV	4.65 Hz
Hay	Block all channels besides h-channel	-76.87 mV	4.65 Hz
Kalmbach	Default (model's only active ion channel is the h-channel)	-78.41 mV	4.65 Hz

(***Silva et al., 1991***; ***Ulrich, 2002***; ***Dembrow et al., 2010***; ***Schmidt et al., 2016***). This behavior is also displayed by some of the neurons making up the population studied by ***Kalmbach et al.*** (***2018***), including the neuron motivating their *in silico* model, in which the implemented h-current model was similar to the rodent h-current model presented by ***Kole et al.*** (***2006***) and used by ***Hay et al.*** (***2011***). The lack of resonance of our L5 Human model, when contrasted to the subthreshold resonance exhibited by the Hay and Kalmbach models, begs the question of what role the differences in h-current kinetics in models might play in dictating this dynamic.

To examine this possibility, we first note that the kinetics of the human h-current model become faster, and in turn closer to what is seen in the rodent model of ***Kole et al.*** (***2006***) (utilized unaltered by ***Hay et al.*** (***2011***)), at more hyperpolarized voltages (see Figure 8). Thus, if we add a hyperpolarizing DC current to the injected ZAP current to lower the value around which the voltage oscillates, different kinetics for the h-current would also be invoked. Figure 10 shows the results of such *in silico* experiments for four different values of this hyperpolarizing DC shift. The impedance plots (the bottom figure in each panel) clearly show that, as the mean voltage becomes more hyperpolarized (as can be seen in the top voltage trace plot by a horizontal black line), the curve

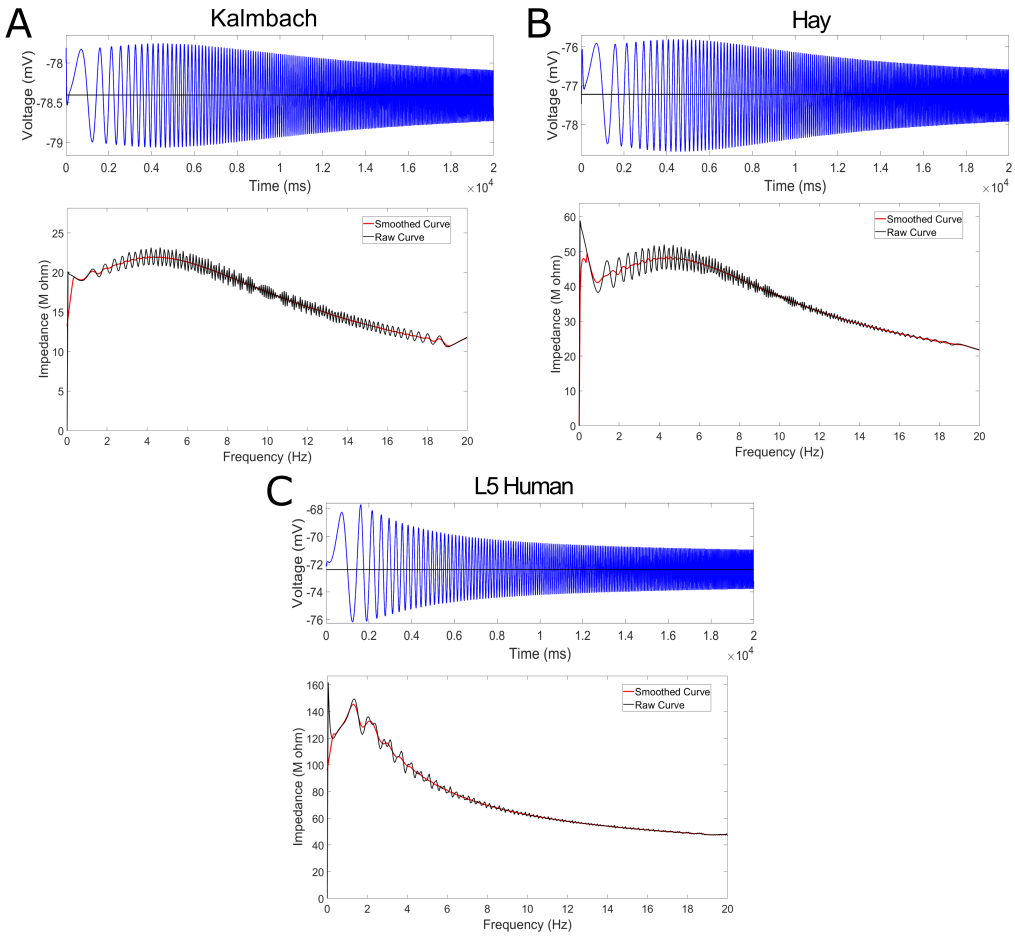

Figure 9. Two pyramidal cell models utilizing h-current kinetics motivated by rodent data each exhibit subthreshold resonance. **(A-C)** Voltage trace (top) and impedance profile (bottom) for the three model pyramidal cells of interest in this study. Previous models from ***Kalmbach et al.*** (***2018***) **(A)** and ***Hay et al.*** (***2011***) **(B)** both exhibit subthreshold resonance, illustrated by a peak in their impedance profiles between 4 and 6 Hz. In comparison, the L5 Human model (**(C)**, replicated from previous Figure 7) does not show this peak.

and the corresponding peak begin shifting rightwards, with an obvious peak appearing in panels **C** and **D**. This resonance is also clearly shown in the corresponding voltage traces.

By comparing the different resting voltages in the protocols presented in Figure 10 (and summarized in Table 3) with the voltage-dependent τ values in the human h-current model (shown in Figure 8), a correlation is apparent between the tendency to exhibit subthreshold resonance and faster h-current kinetics. Indeed, the resonance is most apparent when the L5 Human model oscillates about voltages where the h-current kinetics are as fast, if not faster, than their rodent counterparts (Figure 10**C-D**). While the hyperpolarizing DC shift also elicits higher steady state activation values, our comparisons in this section indicate that subthreshold resonance can arise when the steady state activation value is very low: indeed, the Hay model exhibits subthreshold resonance around a resting membrane potential of approximately -77 mV, where the model has the lowest steady state activation value observed in any of the experiments performed in this exploration (see Figure 8). This subtle but critically important result illustrates that there is a negligible possibility that changes in the steady state activation value might confound the influence of the τ value in dictating subthreshold theta resonance in these experiments.

For comparison purposes, we also perform analogous *in silico* experiments on the Hay and Kalmbach models, with the results summarized in Table 3. In each of these hyperpolarized settings both the Hay and Kalmbach models continue to exhibit subthreshold resonance, as would be

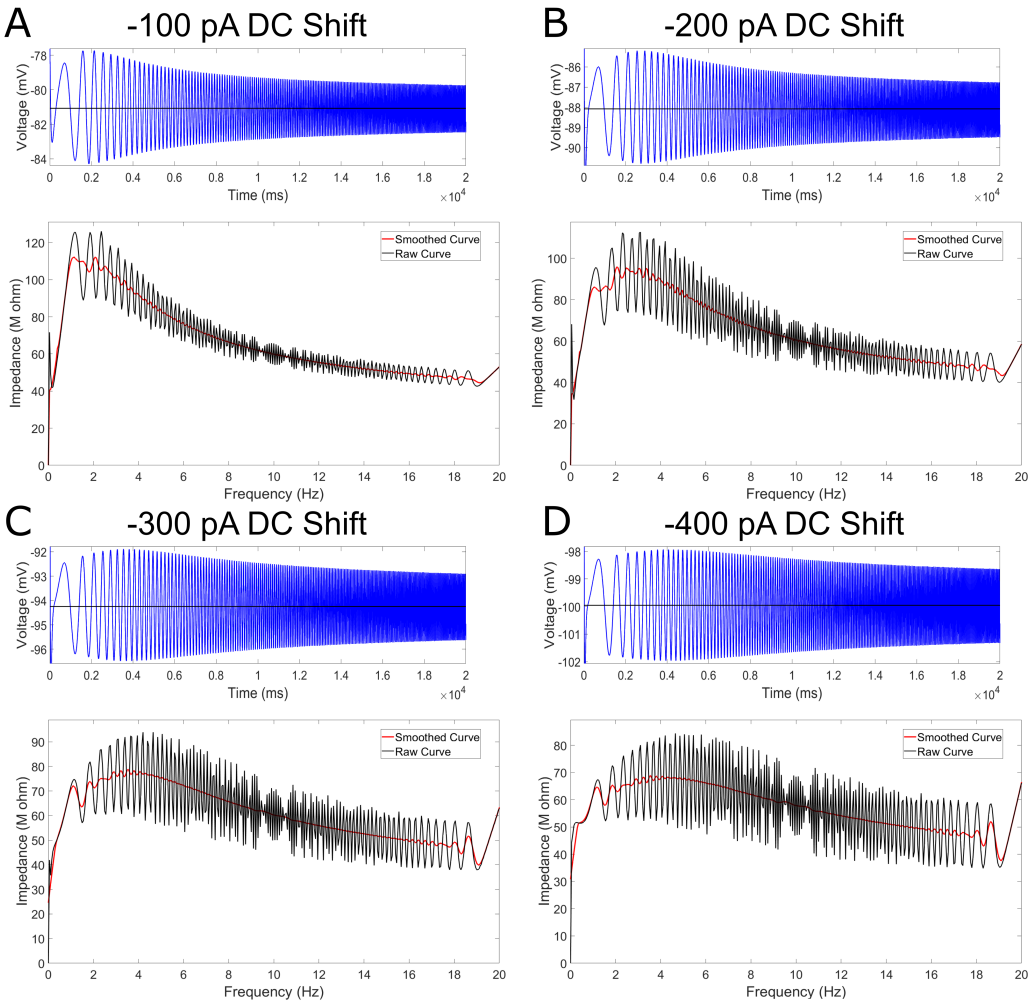

Figure 10. L5 Human model can exhibit subthreshold resonance if held at lower voltages at which the h-current kinetics are faster, implicating these kinetics as playing a crucial role in this dynamic. (A-D) Voltage traces (top) and impedance plots (bottom) for ZAP function protocol identical to that shown in Figure 7 **A-B** with the exception of the addition of DC current to hyperpolarize the cell. DC current is -100 pA in panel **(A)**, -200 pA in panel **(B)**, -300 pA in panel **(C)**, and -400 pA in panel **(D)**. Subthreshold resonance reappears clearly as the membrane potential becomes less than -90 mV, where the kinetics of the h-current are as fast or faster than in the ***Kole et al.*** (***2006***) model (see Figure 6).

expected considering such changes do not affect the kinetics of the h-current in these models as significantly as in the L5 Human model.

We emphasize that there are multiple factors at play in determining whether a neuron exhibits subthreshold resonance, not just the activity of the h-current: indeed, the neuron's morphology, passive properties and other active currents all may play a role (***Hu et al., 2002***; ***Kispersky et al., 2012***). However, we note that using our *in silico* model we are able to more directly address the contribution of the h-current in the neurons' responses to these protocols. In particular, when comparing the L5 Human and Hay models (given that the Kalmbach model only contains the h-current), we find that the h-current is the dominant inward ionic current when the ZAP current is delivered alongside a hyperpolarizing DC current, which is not surprising given the known voltage dependence of the various ionic currents modeled here (see the full equations dictating the various ionic currents' voltage dependencies in ***Hay et al.*** (***2011***)). In fact, the only scenario in which another inward current contributes non-trivially in these *in silico* experiments is when the default L5 Human model is subjected to the ZAP current with no DC current: this is the only case in which the resting

Table 3. Quantified results of the ZAP protocol applied with DC shifts to the three pyramidal cell models of interest (with all included ionic currents active)

Model	DC shift	RMP	Frequency of Peak Impedance (>1 Hz)
L5 Human	-100 pA	-80.96 mV	2.35 Hz
L5 Human	-200 pA	-87.86 mV	3.10 Hz
L5 Human	-300 pA	-93.94 mV	4.65 Hz
L5 Human	-400 pA	-99.52 mV	4.65 Hz
Hay	-100 pA	-81.04 mV	5.45 Hz
Hay	-200 pA	-84.47 mV	5.80 Hz
Hay	-300 pA	-87.55 mV	6.45 Hz
Hay	-400 pA	-90.28 mV	6.75 Hz
Kalmbach	-100pA	-80.28 mV	5.45 Hz
Kalmbach	-200pA	-82.05 mV	5.80 Hz
Kalmbach	-300pA	-83.73 mV	5.80 Hz
Kalmbach	-400pA	-85.34 mV	5.80 Hz

membrane potential of the neuron is high enough to activate another inward current, in this case through the Na_Ta sodium channel. However, considering that, as shown in Table 2, blocking this current does not affect the L5 Human neuron's capacity for resonance, we can reasonably assume that this activity is not playing a major role in dictating this neuron's lack of subthreshold resonance.

In our endeavor to support the hypothesis that a relationship exists between the kinetics of the h-current and a neuron's capacity for subthreshold resonance, the above analysis provides support in one logical "direction": by "speeding up" the kinetics of the h-current in the setting of our L5 Human model, resonance is observed where it previously was not. If we can provide support in the other "direction", namely by showing that "slowing down" the kinetics of the h-current can eliminate resonance where it once was present (i.e. the Hay or Kalmbach models), we will have more complete logical support of our hypothesis. We perform such an investigation via an examination of "hybrid" neural models in which rodent h-current models (that of Hay and Kalmbach) are replaced with the human h-current model; in doing so, the *only* change in a "hybrid" model from its original state is in the kinetics of the h-current. This choice not only achieves the desired logical goal, but also allows for potentially broader conclusions to be drawn regarding human and rodent differences.

Before beginning this investigation, it is important to note that such a switch between human and rodent h-current models would affect other aspects of the cellular model (including, for example, the resting membrane potential, as well as the potential activity of other ion channels) that might affect its behavior. Moreover, the differing morphology and passive properties that make up the "backbones" of these models also differ significantly, and these properties also play a role in dictating a neuron's frequency preference (***Hutcheon and Yarom, 2000***; ***Rotstein and Nadim, 2014***). It is for these reasons that we emphasize that, in performing such a "switch", we create new "hybrid" models that must be approached cautiously. However, a very specific focus on the subthreshold dynamics of these "hybrids" makes their use as presented here reasonable. There are two primary rationales for this assertion: first, a focus on subthreshold dynamics significantly minimizes the role that other ionic currents (whose features vary between "model backbones") will play in the dynamics; and second, by only switching the h-current models (i.e. the kinetics of the h-current), and not the distribution nor conductance of the h-channel, the focus can be mainly on how the different kinetics might play a role (i.e., differences shown in Figure 8).

The results obtained are summarized in Table 4. Most critically we observe that, when the Hay and Kalmbach models have their respective h-current models replaced with the human h-current model, these "hybrids" no longer exhibit subthreshold resonance in response to a default ZAP

protocol (i.e. no DC shift). As the RMPs of these "hybrids" are within the range of voltages for which the human h-current displays significantly slower kinetics than the rodent models, these results are support for the second "direction" in our argument: namely, by "slowing down" the h-current kinetics in the hybrid model as compared to the baseline model, we eliminate the previously observed subthreshold resonance. Doing so in this fashion also further emphasizes the importance of the differences in the human and rodent h-current models in dictating neural dynamics.

Table 4. Quantified results of the ZAP protocol applied to "hybrid" models with and without DC shifts

Model "backbone" from:	H-current model from:	Name of "hybrid" model	DC shift	RMP	Frequency of Peak Impedance (>1 Hz)
Hay	L5 Human	Hay-L5 Human hybrid	0 pA	-72.42 mV	1.45 Hz
Hay	L5 Human	Hay-L5 Human hybrid	-200 pA	-77.94 mV	1.15 Hz
Hay	L5 Human	Hay-L5 Human hybrid	-400 pA	-82.40 mV	3.05 Hz
Kalmbach	L5 Human	Kalmbach-L5 Human hybrid	0 pA	-78.38 mV	1.10 Hz
Kalmbach	L5 Human	Kalmbach-L5 Human hybrid	-200 pA	-81.73 mV	2.30 Hz
Kalmbach	L5 Human	Kalmbach-L5 Human hybrid	-400 pA	-84.70 mV	5.05 Hz

For completeness, we perform analogous experiments with a DC shift on these hybrids as was done on the L5 Human model. As expected, in the "hybrids" in which a rodent h-current model is replaced by the L5 Human h-current model, a hyperpolarizing DC shift can serve to reestablish subthreshold theta resonance, just as in the baseline L5 Human pyramidal cell model. Indeed, with -400 pA DC shifts, both the "Hay-L5 Human" and the "Kalmbach-L5 Human" models show a preferred frequency greater than 3 Hz, and the hyperpolarized resting voltages under these protocols are in a range at which the kinetics of the human h-current approach the kinetics of the rodent h-current models.

Taken together, these results provide crucial support for the argument that the differing h-current kinetics in L5 between humans and rodents play a role in dictating the neural dynamic of subthreshold resonance. This support is bolstered by the dual directions of our causal argument: we can "rescue" resonance by "speeding up" the kinetics of the h-current, and we can "eliminate" resonance by "slowing down" the kinetics of the h-current. The additional fact that eliminating resonance can be achieved by "slowing down" the h-current by imposing human h-current kinetics on a rodent model, thus creating a "hybrid" model, further emphasizes the functional importance of the inter-species differences identified both experimentally and computationally.

Discussion

In this work, we present a biophysically detailed, multi-compartment, full spiking model of a human L5 cortical pyramidal cell that is constrained primarily from morphological and electrophysiological data from the same cell. The model leads to a mathematical characterization of the h-current that is specific to human cortical cells and is validated against experimental data from the primary cell that was not used in model development. Our model additionally mimics subthreshold (a lack of resonance) and general spiking (repetitive spiking frequencies and capacity for PIR spiking) characteristics observed experimentally in a separate population of human L5 cortical pyramidal cells. The fact that the lack of subthreshold resonance was not directly involved in constraining our model indicates that our fitting procedure was able to capture a crucial "essence" of these cells' more complex dynamics, even given the limitations imposed on the modeling process by the data obtained from the primary cell.

This unique computational model allowed us to perform a detailed *in silico* investigation into the relationship between subthreshold resonance and the h-current. This exploration provided convincing support of a strong relationship between the time constant of the h-current's activity and the capacity for subthreshold resonance: such resonance can be "rescued" in cells in which it is

absent by "speeding up" the h-current's kinetics, and "eliminated" in cells in which it is present by "slowing down" the h-current's kinetics. This relationship, combined with the major differences in the speed of the h-current in the human and rodent settings, indicates that there are key functional consequences to the inter-species cellular differences identified in this research.

Multi-compartment human cell model development using a unique data set

All computational models are, in some form, an idealization and abstraction of the physical entity of interest. Given the inherent limitations on such modeling endeavors, the choices of where the necessary approximations are implemented must be made with an overall research question in mind. Such choices should ensure that it is reasonable to use the model to make inquiries into the particular question of interest, which may come at the cost of the model's accuracy or validity in other contexts. Indeed, it is highly unlikely given contemporary tools that an entirely "realistic" neuron model, encapsulating all known properties and dynamics of a biological cell, can ever be obtained; instead, computational neuroscientists must limit the scope of their inquiries and conclusions to the context in which the model was constrained, and is thus the most "realistic" (***Almog and Korngreen, 2016***).

Here, we aimed to make best use of the unique data set motivating this model, namely morphology and a suite of current clamp recordings (in the presence of a voltage-gated sodium channel blocker) obtained from the same human cell. By primarily constraining our model with these data, we minimized the likelihood that cell-to-cell variability could compromise the validity of the model (***Marder and Goaillard, 2006***; ***Golowasch et al., 2002***), especially considering the primary parameters that were optimized were channel conductances (***Goaillard et al., 2009***; ***Ransdell et al., 2013***).

However, naively "fitting" our model to just these current clamp recordings omitted a crucial component of the neuron's function: its spiking characteristics. Given that all recordings from our primary neuron were obtained in the presence of TTX, we could not infer any such characteristics from this primary neuron. This led to the implementation of the informed "cycling" fitting technique schematized in Figure 2. In this fashion, we maintained the benefits of the primary constraining data coming from a single neuron, while also ensuring the neuron retained key spiking characteristics of similarly classified neurons. While this decision brought with it a trade-off in the form of a less accurate fit of the depolarizing current clamp step, retaining these spiking characteristics greatly expanded the realm in which it is "appropriate" to use this model (an example of which can be found in the discussion of frequency-dependent gain below). By well rationalizing each step in the modeling process (see details in the Materials and Methods), we ensured it is appropriate to use our model both in the specific context of analyzing the role of the h-current in subthreshold behaviors, but also in an analysis of how this and other ion channel types might influence general spiking characteristics of human L5 cortical pyramidal cells.

We emphasize that this technique minimizes the potential confounding impact that averaging values, such as passive properties, over multiple cells might have. Indeed, it is well established that the morphology of the neuron plays an important role in dictating its passive properties (***Mohan et al., 2015***; ***Eyal et al., 2016***; ***Beaulieu-Laroche et al., 2018***; ***Gouwens et al., 2018***); as such, imposing passive properties obtained from multiple neurons onto a single morphology in our model is fraught with the potential for error. This is also critical for the h-current, as there is ample evidence in rodents that the h-channel is not distributed uniformly across the dendrites, but rather its density increases exponentially away from the soma (***Ramaswamy and Markram, 2015***; ***Kole et al., 2006***; ***Harnett et al., 2015***); once again, were we to use averages to fit our h-current conductance and kinetics, rather than data from a single cell, the role of the different morphology of each individual cell might impact the "realism" of our final model and its single morphology.

However, as with any modeling endeavor, our cycling technique imposes limitations on the contexts in which the model can be appropriately used. The spiking characteristics constraining model development were limited to repetitive spiking frequencies and the capacity for PIR spiking

observed in a secondary population of L5 pyramidal cells. Thus, any investigation of suprathreshold characteristics of this model must be done with the important caveat that such constraining data did not come from the primary neuron used in model creation. Furthermore, other features of cortical pyramidal cells that might influence the dynamics of human L5 pyramidal neurons, such as the spike shape (***Molnár et al., 2008***), calcium spiking (***Hay et al., 2011***), backpropagating action potentials (***Hay et al., 2011***; ***Larkum et al., 1999***) and synaptic responses (***Molnár et al., 2008***; ***Eyal et al., 2018***) were not used in model creation given the focus on h-current driven dynamics in this study.

In this vein, it is worth emphasizing that the varying density of the h-channel implemented in our model is driven from rodent findings following motivation from the model of ***Hay et al.*** (***2011***) (see details in the Materials and Methods). While there is some experimental evidence that h-channels are similarly distributed in human neurons (***Beaulieu-Laroche et al., 2018***), it is likely that there are some differences in these distributions given the distinct morphologies of similarly classified rodent and human pyramidal neurons. Thus, while we follow the distribution of the rodent h-channel in this model as a necessary strategy given the absence of similarly detailed human data, this is an aspect of the model that may be improved upon as such data becomes available.

Before using the model presented here to probe any of these, or other, features of a human L5 cortical pyramidal cell, some additional "confirmation" must be performed to gauge whether such properties are realistically constrained by the data used in model creation. However, in contexts where the model presented here is not immediately appropriate, "adjustments" based on other experimental data can be made to answer different research questions, just as was done by ***Shai et al.*** (***2015***) in their adjustments to the ***Hay et al.*** (***2011***) model. Indeed, such research is a fertile ground for future work utilizing this model: one potential avenue is better encapsulating the medium afterhyperpolarization (mAHP) implicated in determining a neuron's suprathreshold frequency preference (***Higgs and Spain, 2009***) in order to make the model appropriate for an *in silico* investigation into the different influences the h-current and the mAHP play on these spiking features.

Model comparisons

In this manuscript we compare our human L5 cortical pyramidal cell model with two existing models: the detailed, multi-compartment, rodent L5 cortical pyramidal cell of ***Hay et al.*** (***2011***), and a multi-compartment model of a human cortical deep L3 pyramidal cell with only passive properties and the h-current presented by ***Kalmbach et al.*** (***2018***). Each of these models provides a useful point of comparison, the ***Hay et al.*** (***2011***) model because it is of an analogous rodent neuron with similar computational detail, and the ***Kalmbach et al.*** (***2018***) model because it is constrained by human data.

The ***Hay et al.*** (***2011***) model informed the choice of ion channels implemented in our model (see Materials and Methods) given that it was also of a L5 pyramidal cell, and the optimization of ionic conductances performed by ***Hay et al.*** (***2011***) was similar to our initial optimization method. During model generation we found that a best "fit" to our human experimental data led to significant changes in a variety of conductances (see Table 5) as well as the kinetics of the h-current. Although our model was not constrained by spiking properties such as backpropagating action potentials or calcium spikes like the ***Hay et al.*** (***2011***) model, this choice was motivated by the overall focus in this study on h-current driven dynamics. Considering this emphasis uncovered key inter-species differences, we feel that the model presented here is more suitable for an investigation of distinctly human cortical neuron dynamics.

We note that there exist a variety of other L5 rodent cortical pyramidal cell models (***Keren et al., 2009***; ***Almog and Korngreen, 2014***; ***Farinella et al., 2014***; ***Larkum et al., 2009***) that are focused on features, often concerning spiking behavior, observed in rodent neurons. Thus, while these models may be better suited for *in silico* investigations of these neural dynamics generally speaking, our developed model presented would be much more appropriate to use for an investigation of human

cortical behaviors for the reasons outlined above.

The comparison between our model and other human neuron models is less clear than the conspicuous rodent versus human difference, although the number of these models is severely limited by access to human tissue. ***Beaulieu-Laroche et al.*** (***2018***) present a human L5 cortical pyramidal cell model, but unlike our current work, its morphology was not directly based on a human pyramidal cell. Rather, a modified rat pyramidal neuron morphology was "stretched" to allow comparison to the rodent model of ***Hay et al.*** (***2011***). This model is therefore significantly less detailed morphologically than the one presented here, making direct comparison unjustified. Furthermore, while the Allen Institute is one of few laboratories currently using human data to generate computational neuron models with the level of morphological detail presented here, the human models that are a part of the Allen Brain Atlas (***Dong, 2008***; ***Jones et al., 2009***; ***Sunkin et al., 2012***) at present have their voltage-gated ion channels present only in the somatic regions. The recent model presented by ***Kalmbach et al.*** (***2018***) moves toward the expression of ion channels in dendritic regions, as h-channels are included throughout the dendrites. However, as this is the only voltage-gated ion channel included in the model, it lacks the detail of the model presented here.

The h-current and resonance

H-channels have been a focus of study for many reasons that include their pacemaking and resonant contributions (***Biel et al., 2009***). In particular, the role played by h-currents in dictating subthreshold resonance properties has been examined in excitatory cells (***Hu et al., 2002***, ***2009***; ***Kalmbach et al., 2018***; ***Zemankovics et al., 2010***; ***Silva et al., 1991***; ***Ulrich, 2002***; ***Dembrow et al., 2010***; ***Schmidt et al., 2016***), as well as inhibitory cells (***Kispersky et al., 2012***; ***Zemankovics et al., 2010***; ***Sun et al., 2014***; ***Stark et al., 2013***) both in hippocampus and cortex, and the frequency of this subthreshold resonance has been found to be in the theta frequency range (3-12 Hz). This had led to suggestions of the importance of this feature in theta oscillations in general (e.g., see ***Kispersky et al.*** (***2012***)). However, the relationship between subthreshold and suprathreshold resonant and oscillatory dynamics has yet to be fully articulated: for example, a given subthreshold resonant frequency does not necessarily lead to a similar spiking resonant frequency (***Rotstein and Nadim, 2014***; ***Rotstein, 2017***). The dendritic filtering capacities of neurons (e.g., see ***Vaidya and Johnston*** (***2013***)) further complicates this relationship.

Theoretical and computational studies bring forth the importance of understanding the complexity of the interacting dynamics from different ion channel types and the passive properties in pursuit of better understanding this relationship (***Hutcheon and Yarom, 2000***; ***Rotstein and Nadim, 2014***; ***Rotstein, 2017***). Moreover, the context of the behaving animal (*in vivo*-like) could also affect resonant effects as computationally explored in hippocampal interneurons (***Kispersky et al., 2012***; ***Sekulić and Skinner, 2017***). Thus, whether the h-current is important for the existence of subthreshold resonance should not be considered in a "vacuum", but rather in the context of the multitude of potential insights this dynamic might yield into other functional characteristics both at the single neuron and network levels.

Ongoing and future work

Biophysical predictions of differences in h-current kinetics

H-channels are tetramers that can be either homomeric (consisting entirely of the same subunit type) or heteromeric (consisting of different subunit types) (***Biel et al., 2009***; ***Shah, 2018***). Interestingly, one of the primary differentiating factors between the four subunits are their time constants of activation, with HCN1 subunits being the fastest, HCN4 being the slowest, and HCN2-3 lying in between (***Shah, 2018***).

Viewed in the context of our study, the slower kinetics of the h-current that we observe both computationally and experimentally in human L5 pyramidal neurons (in comparison to their rodent counterparts) suggests that human L5 pyramidal cells might have an increased amount of non-HCN1 subunits amongst their h-channels. Indeed, human neurons in general, and L5 pyramidal

cells specifically, have an enrichment of HCN2 channels as revealed via mRNA expression (***Kalmbach et al., 2018***). HCN2 subunits have slower activation kinetics and a more negative half-activation voltage than HCN1 subunits (***Biel et al., 2009***), with research showing that heteromeric h-channels consisting of a mix of HCN1 and HCN2 subunits display slower kinetics than those seen in HCN1 homomeric h-channels (***Chen et al., 2001***). Taken together, these results provide biophysical support for the hypothesis that the differences in the kinetics of the h-current revealed in this work may be driven by different HCN subunit expression between rodent and human L5 pyramidal neurons.

Indeed, in general resonance is a relatively uncommonly observed phenomenon in human neurons (***Kalmbach et al., 2018***; ***Chameh et al., 2019***), which may be due to the greater expression of HCN2 channels in human neurons generally (***Kalmbach et al., 2018***). A detailed comparison between subunit expression in rodents and humans remains wanting given the clear predictions of this study. Additionally, since channel kinetics can be altered by post-translation modification, proteomics may be helpful in investigating post-translation modification of HCN subunits in human neurons.

Toward a better understanding of frequency-dependent gain in human L5 cortical pyramidal neurons

In characterizing a large population of human L5 cortical pyramidal neurons, ***Chameh et al.*** (***2019***) investigated both subthreshold and suprathreshold dynamics. The frequency-dependent gain (described in detail in the Materials and Methods) measure developed by ***Higgs and Spain*** (***2009***) encapsulates a cell's phase preference for spiking in response to an oscillatory input as a function of frequency. While such suprathreshold behaviors were not a focus of this modeling endeavor, given the availability of this experimental data for comparison purposes we applied an analogous *in silico* protocol to our model neuron.

Interestingly, despite frequency-dependent gain not being used in our model development, our L5 Human model still captures some key features observed experimentally in the frequency-dependent gain. As shown in Figure 11, the general shape of the frequency-dependent gain curve is similar in the model (panel **A**) and experimental (panel **B**) settings, in particular matching the peak in the 3-4 Hz range and the valley in the 5-10 Hz range. This correspondence further expands the realm in which it might be appropriate to utilize this model in future work; for example, a computational exploration may be uniquely suited to isolate the contribution of the h-current to suprathreshold frequency preference.

Methods and Materials

Experimental recordings of human L5 cortical pyramidal cells

Ethics statement

Surgical specimens were obtained from Toronto Western Hospital. Written informed consent was obtained from all study participants as stated in the research protocol. In accordance with the Declaration of Helsinki, approval for this study was received by the University Health Network Research Ethics board.

Acute slice preparation from human cortex

Neocortical slices were obtained from the middle temporal gyrus in patients undergoing a standard anterior temporal lobectomy for medically-intractable epilepsy (***Mansouri et al., 2012***). Tissue obtained from surgery was distal to the epileptogenic zone tissue and was thus considered largely unaffected by the neuropathology. We note that this is the same area from which recent data characterizing human L3 cortex was obtained (***Kalmbach et al., 2018***).

Immediately following surgical resection, the cortical block was placed in an ice-cold (approximately 4°C) slicing solution containing (in mM): sucrose 248, KCl 2, MgSO4.7H2O 3, CaCl2.2H2O 1, NaHCO3 26, NaH2PO4.H2O 1.25, and D-glucose 10. The solution was continuously aerated with

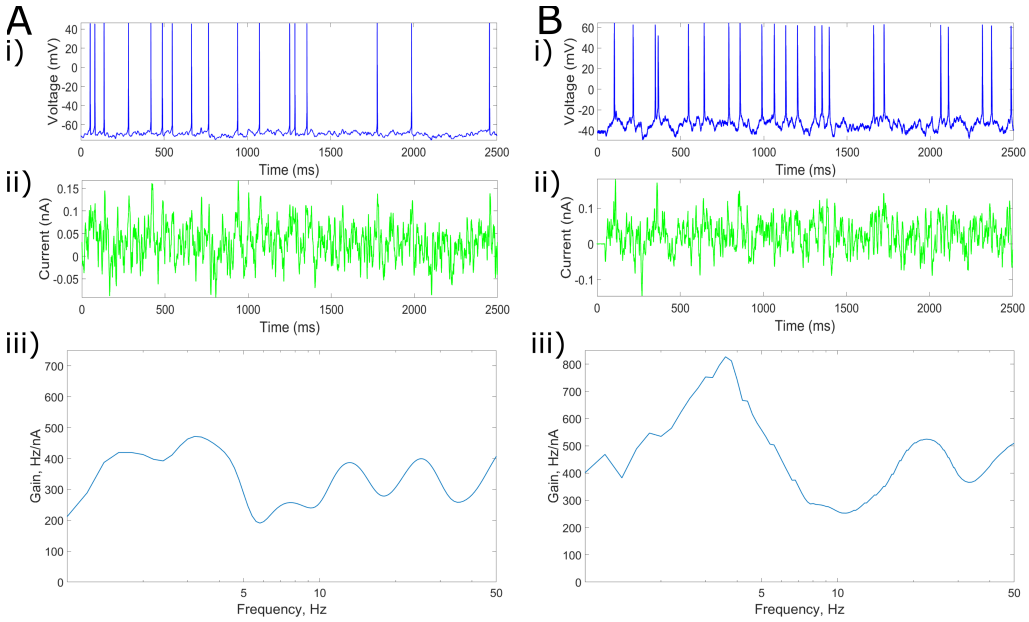

Figure 11. Model mimics crucial frequency-dependent gain properties observed experimentally in human L5 pyramidal neurons. **(A)** *In silico* results from the model neuron to the application of Gaussian-filtered white noise with a gain of 40 pA and a DC current chosen so that the neuron spikes at theta (4-10 Hz) frequency. An example voltage trace is shown in **i)**, the corresponding noisy input current in **ii)**, and the frequency-dependent gain (averaged over sixty different noisy inputs) in **iii)**. **(B)** Example *in vitro* results of an analogous frequency-dependent gain protocol (plots correspond with those in panel **A**). While the amplitude of the gain is higher in this plot (which can be explained by the firing being in the high theta, as opposed to low theta, range), the general shape of the frequency-dependent gain plot (namely the freqencies at which peaks and valleys occur) largely corresponds with the *in silico* results.

95% O2-5% CO2 and its total osmolarity was 295-305 mOsm. Tissue blocks were transported to the laboratory within 5 min. Transverse brain slices (400 μm) were cut using a vibratome (Leica 1200 V) in slicing solution. Tissue slicing was performed perpendicular to the pial surface to ensure that pyramidal cell dendrites were minimally truncated (***Kostopoulos et al., 1989***; ***Kalmbach et al., 2018***). The slicing solution was the same as used for transport of tissue from the operation room to the laboratory. The total duration of transportation and slicing was kept to a maximum of 20 minutes, as suggested by ***Köhling and Avoli*** (***2006***).

After sectioning, the slices were incubated for 30 min at 34°C in standard artificial cerebrospinal fluid (aCSF). The aCSF contained (in mM): NaCl 123, KCl 4, CaCl2.2H2O 1, MgSO4.7H2O 1, NaHCO3 25, NaH2PO4.H2O 1.2, and D-glucose 10, pH 7.40. All aCSF and slicing solutions were continuously bubbled with carbogen gas (95% O2-5% CO2) and had an osmolarity of 295-305 mOsm. Following this incubation, the slices were kept in standard aCSF at 22–23°C for at least 1 h, until they were individually transferred to a submerged recording chamber.

For the subset of experiments designed to assess frequency dependent gain, slices were prepared using the NMDG protective recovery method (***Ting et al., 2014***). The slicing and transport solution was composed of (in mM): NMDG 92, KCl 2.5, NaH2PO4 1.2, NaH2PO4.H2O 30, HEPES 20, Glucose 25, Thiourea 2, Na L-ascorbate 5, Na-Pyruvate 3, CaCl2.2H2O 0.5, and MgSO4.7H2O 10. The pH of NMDG solution was adjusted to 7.3-7.4 using hydrochloric acid and the osmolarity was 300-305 mOsm. Before transport and slicing, the NMDG solution was carbogenated for 15 min and chilled to 2-4 °C. After slices were cut (as described above), they were transferred to a recovery chamber filled with 32-34 °C NMDG solution continuously bubbled with 95% O2-5% CO2. After 12 minutes, the slices were transferred to an incubation solution containing (in mM): NaCl 92, KCl 2.5, NaH2PO4.H2O 1.2, NaHCO3 30, HEPES 20, Glucose 25, Thiourea 2, Na L-ascorbate 5, Na-Pyruvate 3, CaCl2.2H2O 2, and MgSO4.7H2O 2. The solution was continuously bubbled with 95%

O2 -5% CO2. After a 1-hour incubation at room temperature, slices were transferred to a recording chamber continuously perfused with aCSF containing (in mM): NaCl 126, KCl 2.5, NaH2PO4.H2O 1.25, NaHCO3 26, Glucose 12.6, CaCl.H2O 2, and MgSO4.7H20 1.

Electrophysiological recordings

Motivation for and limitations of the focus on recordings from a single neuron. Access to human tissue provided no control over age, gender, or the particular aspect of the surgery involved, which only adds to the issue of experimental variability in recording between similarly classified cells. This, along with the issues presented by "cell-to-cell variability" discussed previously (***Golowasch et al., 2002***), motivated the choice to obtain as much electrophysiological data as possible from the same human L5 cortical pyramidal neuron.

While this choice is well-rationalized, there are limits to the amount of applicable data that can be obtained from a single cell. Indeed, in patch-clamp experiments (described below), key properties of the neuron (including, for example, the axial resistance) decay with time. We thus focused our modeling on a primary cell from which we obtained a good fill (for morphological reconstruction, described below) and a large and reliable set of recordings for model building and parameter fitting. This was a set of current clamp data obtained in the presence of TTX to block action potential firing (described in detail below) and voltage clamp data from this cell under the same setting.

It is worth emphasizing that, given limitations to our experimental protocol imposed by the use of human tissue, we were unable to perform voltage clamp experiments both with and without the h-channel blocker ZD in the same cell to truly "isolate" the h-current. This crucial factor helped to motivate the decision to use current clamp data to constrain our model; along with the issues of the space-clamp and maintaining self-consistency in the modeling process as described previously, without ZD recordings we can not assert with full certainty that the h-current features derived from voltage clamp data are not influenced by other channels. It is for this reason that this data was used for model validation, in which these "approximate" values of the h-current kinetics are more appropriate, rather than direct model constraint.

To supplement the data from the primary neuron, we made use of averaged experimental data from multiple secondary cells. This provided the data of Table 1, which are averaged data from 147 cells, and the mean $\pm$ standard deviation plots in Figure 6. For the data in Figure 6, we note that for τ values, the values between -70 and -110 mV are averaged over 14 neurons, while the remaining values are averaged over 5 neurons. For the steady state activation plot, values between -150 and -70 mV are averaged over 14 neurons, while the extreme values at -160 and -60 mV are averaged over 5 neurons. The details in how these values were derived from voltage clamp experiments are included in the following.

Experimental setting. *In vitro* whole-cell recordings were obtained from human neocortical L5 neurons. For recording, slices were transferred to a recording chamber mounted on a fixed-stage upright microscope (Axioskop 2 FS MOT; Carl Zeiss, Germany), and were continually perfused at 8 ml/min with standard aCSF at 32-34 oC. All experiments were performed with excitatory (APV 50 μM, Sigma; CNQX 25 μM, Sigma) and inhibitory (Bicuculline 10 µM, Sigma; CGP-35348 10 μM, Sigma) synaptic activity blocked. Cortical neurons were visualized using an IR-CCD camera (IR-1000, MTI, USA) with a 40x water immersion objective lens.

Patch pipettes (3-6 MΩ resistance) were pulled from standard borosilicate glass pipettes (thin-wall borosilicate tubes with filaments, World Precision Instruments, Sarasota, FL, USA) using a vertical puller (PC-10, Narishige). Pipettes were filled with intracellular solution containing (in mM): K-gluconate 135, NaCl 10, HEPES 10, MgCl2 1, Na2ATP 2, GTP 0.3, and biocytin (3-5mg/mL). The solution's pH was adjusted with KOH to 7.4 and its osmolarity was 290–300 mOsm. Whole-cell patch-clamp recordings were obtained with an Multiclamp 700A amplifier and pClamp 9.2 data acquisition software (Axon instruments, Molecular Devices, USA). Subsequently, electrical signals were digitized at 20 kHz using a 1320X digitizer. The access resistance was monitored throughout

the recording (typically between 8-25 MΩ), and cells were discarded if access resistance was > 25 MΩ. The liquid junction potential was calculated to be 10.8 mV which is corrected for whenever the experimental data is used for modeling or in direct comparison to model values (i.e. Figure 6), but not when the experimental data is presented on its own (i.e. Figure 7**B** and **D**).

Current clamp data directly constraining computational modeling Current clamp data used as the primary constraint for the computational model presented here was obtained from the primary cell in the following fashion. Hyperpolarizing current pulses (1000 ms duration, -50-400 pA, step size: 50 pA) and depolarizing current pulses (1000 ms duration, 50-400 pA/ step size: 50 pA) were injected to measure passive and active membrane properties in presence of voltage gated sodium channels blocker (TTX 1 μM; Alomone Labs). This data is highlighted in Figure 1.

Characterization of h-current kinetics using voltage clamp data. To characterize the h-current kinetics, 1000 ms-long voltage clamp steps were used in -10 mV increments, down to -140 mV from a holding potential of -60 mV. The tail current was quantified as the difference between peak amplitude of residual current at the end of each holding potential and the steady state current from holding potentials of -140 to -60 mV. This value was used to calculate the steady-state activation curve as presented in Figure 6 by normalizing these values between 0 and 1. To calculate the time constant of the h-current, a single or double-exponential model was fitted to the initial response of the neuron to the voltage clamp using Clampfit 10.7 (Molecular devices). In experiments quantifying the h-current kinetics, tetrodotoxin (TTX, 1 µM; Alomone Labs) to block voltage gated sodium currents, CoCl2 (2mM; Sigma-Aldrich) to block voltage-sensitive calcium currents, and BaCl2 (1mM; Sigma-Aldrich) to block inwardly rectifying potassium current were added to the bath solution. These recordings were taken both in the primary cell and in secondary L5 pyramidal cells, the data for both of which are presented in Figure 6.

Spiking data. To characterize general repetitive and post-inhibitory rebound spiking characteristics of human L5 cortical pyramidal cells, current clamp recordings were taken without TTX in secondary cells. The duration of the current pulse was 600 ms. This data, as presented in Table 1, was obtained from 147 cells.

Histological methods and morphological reconstruction

During electrophysiological recording, biocytin (3-5 mg/ml) was allowed to diffuse into the patched neuron; after 20-45 min, the electrodes were slowly retracted under visual guidance to maintain the quality of the seal and staining. The slices were left for another 10-15 min in the recording chamber to washout excess biocytin from the extracellular space, then slices containing biocytin-filled cells were fixed in 4% paraformaldehyde in PBS for 24 hours at 4°C. The slices were washed at least 4×10 min in PBS solution (0.1 mM). To reveal biocytin, slices were incubated in blocking serum (0.5% Bovine serum albumin (BSA), 0.5% milk powder) and 0.1% Triton X-100 in PBS for 1 hour at room temperature.

Finally, slices were incubated with streptavidin fluorescein (FITC) conjugated (1:400) (Thermo Fisher Scientific, Canada) on a shaker at 4°C for 12 hours. Then slices were washed at least 4×10 min in PBS and mounted on the glass slide using moviol (Sigma-Aldrich). Imaging was done using a Zeiss LSM710 Multiphone microscope. Cellular morphology was reconstructed using IMARIS software (Bitplane, Oxford instrument company). These steps were performed on the same neuron from which the current clamp traces were obtained, yielding the morphology shown in Figure 1.

The number of compartments in the final reconstruction of the primary human L5 pyramidal cell was 211. This was verified to be numerically appropriate in simulations performed.

Subthreshold resonance

To assess the subthreshold resonance properties of L5 pyramidal cells, a frequency modulated sine wave current input (ZAP) was generated ranging from 1 to 20 Hz, lasting 20 s (***Hutcheon et al., 1996***) with a sampling rate of 10 kHz. This current waveform was then injected using the custom waveform feature of Clampex 9.2 (Axon Instruments, Molecular devices, USA). The subthreshold

current amplitude was adjusted to the maximal current that did not elicit spiking. The impedance curve resulting from this experiment was calculated as illustrated by ***Puil et al.*** (***1986***). Summarized briefly, the impedance is calculated by dividing the power spectrum of the voltage trace by the power spectrum of the current trace under a ZAP protocol. Given the noisiness of these plots, in our presentations we also include a “smoothed" version of these curves simply calculated using the *smooth* function in MATLAB (***MATLAB, 2019***).

Frequency Dependent Gain

Following a similar methodology of ***Higgs and Spain*** (***2009***), frequency dependent gain was computed using 30 trials (inter-trial interval = 20s) of a 2.5s duration current injection stimulus of frozen white noise convolved with a 3 ms square function (***Galán et al., 2008***). The variance of the noise, along with the tonic DC current, was chosen to elicit spike rates in the 5-10 Hz range, which is typical for cortical pyramidal cells (***Neske and Connors, 2016a***,b). The amplitude, or variance of the current injection stimulus was scaled to elicit spike rates of above 5 Hz the typical firing rate for cortical pyramidal cells (***Neske and Connors, 2016a***,b). In addition to increasing the noise variance, a steady amount of DC current was required (***Higgs and Spain, 2009***) to elicit spiking which was delivered as various amplitude steps added to the noisy current input. Peaks detected in the voltage time series with overshoot greater than 0 mV were taken to be the occurrence of an action potential. The time varying firing rate r(t) was given by:

$$r(t) = \begin{cases} \frac{1}{\Delta t} & \text{When spike detected} \\ 0 & \text{When no spike detected} \end{cases} \quad (1)$$

The gain was then calculated as:

$$G(f) = \frac{C_{sr}(f)}{C_{ss}(f)} \quad (2)$$

where the C functions represent the complex Fourier components of the stimulus-response correlation (sr) and the stimulus autocorrelation (ss) as defined in ***Higgs and Spain*** (***2009***).

The noisy current is applied to the neuron 30 times, with the final $G(f)$ curve the averaged response over these 30 trials (as presented in Figure 11**Biii**).

Construction of multi-compartment computational model of a human L5 cortical pyramidal cell

The code containing the final model, as well as various tools to perform *in silico* experiments, can be found at https://github.com/FKSkinnerLab/HumanL5NeuronModel. We describe the development of this model below.

Ionic currents

The ion channel types and distributions in a previous detailed, multi-compartment model of a rodent L5 pyramidal cell model (***Hay et al., 2011***) were used as a basis for developing our human L5 pyramidal cell model. Thus the human L5 pyramidal cell model, before any adjustments or parameter optimization, consisted of the same 10 ion channel types producing the ionic currents present in the multi-compartment model. These are listed in the Results section.

Mathematical equations and parameter values

The mathematical equations describing the currents used a conductance-based formalism and kinetics for each of these channels in our human L5 pyramidal cell model was unaltered except for Ih, Na_Ta, and SKv3_1. These equations and kinetic parameters are given in the Methods of ***Hay et al.*** (***2011***).

The Ih kinetics were fit from scratch to allow for any potential differences between rodent and human h-currents to be captured. We used a general mathematical model structure as used in

previous work to model h-current dynamics (***Sekulić et al., 2019***) and included the parameters in this model in our optimizations.

The equations for the h-current model are as follows:

$$\begin{aligned} i_{hcn} &= \text{glh} * (v - ehcn) \\ \text{glh} &= \text{glhbar} * m \\ \frac{dm}{dt} &= (m_\infty - m)/m_\tau \\ m_\infty &= 1/(1 + e^{((v-vh)/k)}) \\ m_\tau &= f + 1/(e^{-a-b*v} + e^{-c+d*v}) \end{aligned} \tag{3}$$

where i_{hcn} is the current flow through the h-channels in mA/cm^2, glh is the conductance in S/cm^2, v is the voltage in mV, glhbar is the maximum conductance in S/cm^2 (an optimized parameter), m is the unitless gating variable, t is time (in ms), vh is the half-activation potential (an optimized parameter, in mV), $ehcn$ is the reversal potential for this channel (an optimized parameter, in mV) k is the slope of activation (an optimized parameter), and a, b, c, d and f are optimized parameters (in ms). m_∞ is the steady-state activation function and m_τ is the time constant of activation.

The changes to the Na_Ta and SKv3_1 ionic currents were simple "shifts" of the activation curves to more hyperpolarized voltages, as necessitated to best replicate experimentally measured post-inhibitory rebound and repetitive firing characteristics of human L5 cortical pyramidal cells as in Table 1. The specific equations where these changes are implemented are shown below:

$$\begin{aligned} i_{NaTa} &= \text{gNaTa} * (v - ena) \\ \text{gNaTa} &= \text{gNaTabar} * m * m * m * h \\ \frac{dm}{dt} &= (m_\infty - m)/m_\tau \\ \frac{dh}{dt} &= (h_\infty - h)/h_\tau \\ m_\alpha &= \frac{0.182 * (v - (-38 - shift_{Na\_Ta}))}{1 - (\exp(-(v - (-38 - shift_{Na\_Ta}))/6))} \\ m_\beta &= \frac{0.124 * (-v + (-38 - shift_{Na\_Ta}))}{1 - (\exp(-(v + (-38 - shift_{Na\_Ta}))/6))} \\ m_\tau &= \frac{1}{m_\alpha + m_\beta}/qt \\ m_\infty &= \frac{m_\alpha}{m_\alpha + m_\beta} \\ h_\alpha &= \frac{-0.015 * (v - (-66 - shift_{Na\_Ta}))}{1 - (\exp((v - (-38 - shift_{Na\_Ta}))/6))} \\ h_\beta &= \frac{-0.015 * (-v + (-66 - shift_{Na\_Ta}))}{1 - (\exp((-v + (-38 - shift_{Na\_Ta}))/6))} \\ h_\tau &= \frac{1}{h_\alpha + h_\beta}/qt \\ h_\infty &= \frac{h_\alpha}{h_\alpha + h_\beta} \end{aligned} \tag{4}$$

where qt is a local constant equal to $2.3^{(34-21)/10}$;

$$\begin{aligned} i_{SKv3\_1} &= \text{SKv3\_1} * (v - ek) \\ \text{gSKv3\_1} &= \text{gSKv3\_1bar} * m \\ \frac{dm}{dt} &= (m_\infty - m)/m_\tau \\ m_\tau &= \frac{0.2 * 20.000}{1 + \exp(((v - (-46.560 - shift_{SKv3\_1}))/-44.140))} \\ m_\infty &= \frac{1}{1 + \exp(((v - (18.700 - shift_{SKv3\_1}))/-9.7))} \end{aligned} \tag{5}$$

The units of the i (current), g (conductance), v (voltage), e (reversal potential), and t (time) terms in both of these equations are as given above for the h-current. ena refers to the reversal potential of sodium and ek refers to the reversal potential of potassium, both of which are unaltered from ***Hay et al.*** (***2011***). m and h remain unitless gating variables in both equations. The $shift$ parameters have units of mV.

Values of the maximum conductances associated with each of these currents in the Hay model and in our L5 Human model are given in Table 5.

Table 5. Parameters for the L5 Human model, with maximum conductances and passive properties compared to the Hay model.

Ionic Current	**L5 Human Model maximum conductance** (nS/cm^2)	**Hay Model maximum conductance** (nS/cm^2)
Na_Ta (soma)	2.2	2.04
Na_Ta (apical)	0.001	0.0213
Nap_Et2	1e-06	0.00172
K_Pst	0.07	0.00223
SKv3_1 (soma)	0.04	0.693
SKv3_1 (apical)	0.04	0.000261
SK_E2 (soma)	2.0964e-09	0.0441
SK_E2 (apical)	2.0964e-09	0.0012
K_Tst	2e-05	0.0812
Ca_LVA (soma)	0.00099587	0.00343
Ca_LVA (apical)	0.00099587	0.0187
Ca_HVA (soma)	1.7838e-09	9.92e-04
Ca_HVA (apical)	1.7838e-09	0.000555
Ih (soma, basilar)	5.0723e-05	2e-04
Im	2e-04	6.75e-05
Passive Property Parameter	**L5 Human Model Value**	**Hay Model Value**
Ra, ohm cm	501.6	100
e_pas, mV	-84.325	-90
cm (soma), uF/cm^2	1	1
cm (apical), uF/cm^2	1.6226	2
cm (basilar), uF/cm^2	1.6226	2
cm (axonal), uF/cm^2	1.6226	1
g_pas (soma), nS/cm^2	1.75e-05	3.38e-05
g_pas (apical), nS/cm^2	1.75e-05	5.89e-05
g_pas (basilar), nS/cm^2	1.75e-05	4.67e-05
g_pas (axonal), nS/cm^2	1.75e-05	3.25e-05

H-current Parameter	**L5 Human Model Value**
a, ms	23.428
b, ms	0.21756
c. ms	1.3881e-09
d, ms	0.082329
f, ms	1.9419e-09
k	8.0775
vh, mV	-90.963
ehcn, mV	-49.765
"Shift" Parameter	**Value**
$shift_{Na\_Ta}$, mV	-5
$shift_{SKv3\_1}$, mV	-10

Ion channel distributions

The locations of each of the 10 ion channel types in our human L5 pyramidal cell model are summarized in Table 6, and utilize a classification of each compartment in the neuron model as part of the soma, apical or basilar dendrites. With three exceptions, the ion channels were distributed as in the model of ***Hay et al.*** (***2011***).

The first and second exceptions are the calcium channels (Ca_HVA and Ca_LVA currents). A feature of the ***Hay et al.*** (***2011***) model that required adjustment was the “calcium hot spot". As described by ***Hay et al.*** (***2011***) and ***Larkum and Zhu*** (***2002***), experimental evidence suggests a region of increased calcium channel conductance near the “main bifurcation” in the apical dendrites in rodent L5 pyramidal cells. The location of this bifurcation is closer to the soma in the morphology of

the human L5 pyramidal cell than that used in ***Hay et al.*** (***2011***) considering the difference between human and rodent cell morphology, even in similar brain regions (***Beaulieu-Laroche et al., 2018***). As such the region of this increased calcium activity, where the Ca_LVA maximum conductance is multiplied by 100 and the Ca_HVA maximum conductance is multiplied by 10, is chosen to be on the apical dendrite 360 to 600 microns from the soma.

The third exception are the h-channels. The function used to model the "exponential distribution" of h-channels along the dendrites (***Kole et al., 2006***; ***Ramaswamy and Markram, 2015***; ***Beaulieu-Laroche et al., 2018***) was also slightly adjusted from that presented in ***Hay et al.*** (***2011***) given the distinct neuron morphology of the primary cell used here. For a given apical dendritic compartment, the maximum conductance of the h-current, gIhbar*, is given by the following equation:

$$\text{gIhbar*} = \text{gIhbar} \times \left(-0.8696 + 2.0870 \times e^{3.6161 \times \left(\frac{\text{dist}}{1000} \right)} \right) \tag{6}$$

where "dist" is the distance from the soma to the midway point of the given compartment, the denominator of "1000" is chosen since this is the approximate distance from the soma to the most distal dendrite, and "gIhbar" is the h-current maximum conductance value that is optimized. "gIhbar" is also the value of the maximum conductance in the soma and basilar dendrites (i.e. the Ih maximum conductance is constant across all compartments in these regions).

Table 6. Summary of the distribution of ion channels in the differently classified compartments in the human L5 cortical pyramidal cell model.

Type	Location	Ion Channel Distribution Notes
Na_Ta	Soma, apical dendrites	Different maximum conductance values in soma and apical dendrites
Nap_Et2	Soma	
K_Pst	Soma	
SKv3_1	Soma, apical dendrites	
SK_E2	Soma, apical dendrites	
K_Tst	Soma	
Ca_LVA	Soma, apical dendrites	Exhibits "calcium hot spot" in apical dendrite (maximum conductance multiplied by 100 between 360 and 600 microns from soma)
Ca_HVA	Soma, apical dendrites	Follows "calcium hot spot" in apical dendrite (maximum conductance multiplied by 10 between 360 and 600 microns from soma)
Ih	Soma, apical dendrites, basilar dendrites	Follows exponential distribution in apical dendrites (see Equation 6, where gIhbar is set to the Ih maximum conductance in the soma and basilar dendrites)
Im	Apical dendrites	

Details of the cycling fitting strategy

Parameter optimization using NEURON's Multiple Run Fitter algorithm

The first step in the "cycling" model development strategy (schematized in Figure 2) utilized NEURON's built in Multiple Run Fitter (MRF) algorithm for optimization (***Hines and Carnevale, 2001***; ***Carnevale and Hines, 2006***). This algorithm utilizes the PRAXIS method to minimize the error between the output (in this case, a voltage trace) of the model neuron in comparison to experimental data obtained from an analogous protocol (***Brent, 1976***). Here, we fit the model to five different

current clamp protocols experimentally obtained from the primary neuron from which we obtained our human L5 cell morphology. As the experimental current clamp data was obtained in the presence of TTX, all sodium conductances were set to zero and not altered in this step. Additionally, the potassium channel currents primarily involved in action potential generation, K_Pst and SKv3_1, were omitted from the optimization and "hand-tuned" in the second step of the cycle.

We chose to use three hyperpolarizing current clamp traces, with -400 pA, -350 pA, and -300 pA current amplitudes, because at these hyperpolarized voltages it was reasonable to assume that the h-current was primarily responsible for the voltage changes (***Toledo-Rodriguez et al., 2004***). This allowed us to accurately fit not only the h-current maximum conductance, but also its kinetics (see Equation 3 above).

A hyperpolarizing current step with a small (-50 pA) magnitude was chosen to constrain the passive properties, as near the resting membrane potential it is primarily these properties that dictate the voltage responses ("charging" and "discharging") to a current clamp protocol. We note that this trace does not represent a perfectly "passive" neuron, as some conductances (such as those due to the h-current) are active, albeit minimally, at mildly hyperpolarized voltages (only the sodium channels were directly blocked in this protocol, via the application of TTX). Nonetheless, given that our model fit this current clamp data well, and also mimicked the "charging" and "discharging" portions of all the current clamp protocols included in the optimization, we are confident that we accurately approximated the passive properties of our particular human L5 pyramidal neuron. The final passive properties are shown in Table 5 along with those of a rodent L5 cortical pyramidal cell model of ***Hay et al.*** (***2011***). The passive properties include Ra (the axial resistivity in ohm cm), e_pas (the passive reversal potential in mV), cm (the specific capacitance in uF/cm^2), and g_pas (the passive conductance in S/cm^2).

Finally, a depolarizing current step (100 pA) was chosen to ensure the model was not "overfit" to the hyperpolarized data. Early in the modeling process, we recognized that a "best fit" of the depolarizing current clamp data would involve minimizing the values of the K_Pst and SKv3_1 maximum conductances to the point that action potential generation would not be viable. It is for this reason that the "cycling technique" was developed to ensure that reasonable spiking characteristics were achieved by the model while also minimizing these conductances as much as possible to best fit the depolarizing current clamp trace.

We note that, in the process of designing this modeling technique, we chose not to use every current clamp recording available to us, but instead chose a moderate number of current clamp recordings for use in the optimization. This is due to computational considerations and a desire for the modeling technique to be potentially applicable in other settings using reasonable computational resources and computational time spent.

A useful tool provided by NEURON's MRF is the ability to differentially "weigh" portions of the traces in the computation of the error value we sought to minimize. Given the focus of this study was on uncovering dynamics of the h-current, we more heavily weighed the portions of the voltage trace in which this channel most affected the voltage, namely the initial "sag" following a hyperpolarizing current steps and the "rebound" in voltage when this inhibition is released. We also chose portions of the voltage trace to emphasize in the error calculation in order to ensure the model cell closely approximated the resting membrane potential observed experimentally, as well as matched the "charging" and "discharging" features heavily influenced by passive properties.

We note that these differential "weights" were chosen only after a rigorous exploration of how these choices affected the overall model fit; indeed, this choice yielded a model that both qualitatively and quantitatively best fit the experimentally-observed behavior of our human L5 cortical pyramidal cell. We also note that the possibility that our final parameters represented a "local", rather than "global" minimum in the optimization was investigated by running the optimization with a variety of initial conditions; the solution with the minimum error from all of these trials is the one presented here.

Matching of spiking features

After optimizing the parameters using MRF, we then tuned the sodium and potassium conductances involved in action potential generation by hand in order to achieve PIR and repetitive spiking behaviors reasonably approximating that seen in experiments (and summarized in Table 1). As described above, we sought to achieve this reasonable behavior while minimizing the relevant potassium conductances so as to best fit the 100 pA current clamp trace.

In this step, we also found that a "shift" in the activation curve for Na_Ta (see Equation 4 above) was necessary to achieve PIR spiking as seen experimentally. We sought to minimize this shift for simplicity, but also because a side effect of this leftward shift was an increase in repetitive firing frequency that approached the upper limit of what was biologically reasonable. We note that the final shift of -5 mV kept the dynamics of our sodium channel well within a reasonable range (for example, the sodium channel used in the model presented by ***Ascoli et al.*** (***2010***) has a significantly more leftward shifted sodium activation curve than our model).

Finally, in order to prevent biologically unrealistic depolarization blocks from occurring in our model (since these are not seen experimentally), we shifted the activation curve for SKv3_1 more leftward (-10 mV) than the sodium channel (see Equation 5 above). This technique for preventing depolarization block in computational models has been previously suggested by ***Bianchi et al.*** (***2012***).

Final model parameters

The "cycling" mechanism described in detail above was run until there was no significant improvement in the quantitative (i.e. the "error" in the optimization step) or qualitative (i.e. the spiking characteristics) measurement of model accuracy in either step of the cycle. The resulting parameter choices are summarized in Table 5, shown together with those of a rodent L5 pyramidal cell as developed by ***Hay et al.*** (***2011***).

The input resistance of the final model was 82.48 Mohm which compares favourably with the experimental data from the primary cell which yields an input resistance of 82.08 Mohm. This correspondence is as expected given the accurate fits that drove the modeling process. These values were determined by performing a linear fit (with a fixed y-intercept of 0) between an input current ("x value") and the resulting steady-state change in voltage ("y value") for input currents of -200, -150, -100, -50, 0, 50, and 100 mV.

The membrane time constant of our final model was 36.76 ms, which compares favourably with the experimental data from the primary cell which yields a membrane time constant of 32.69 ms. Again, this correspondence is as expected given the accurate fits that drove the modeling process. These values were determined by fitting a double-exponential equation ($a * e^{b*x} + c * e^{d*x}$) to the discharging portion of the voltage trace in response to the -50 pA current clamp, with the membrane time constant being the constant corresponding with the "slow" exponent (i.e. the value of b or d that was smaller in magnitude).

Parameter constraints

Moderate constraints were placed on the range of certain parameters in order to ensure that, in finding the best "fit" to the data, these values did not enter a regime known to be biologically unlikely or that would lead to unreasonable spiking characteristics. In order to preserve reasonable spiking behavior, the maximum value for the Ca_LVA maximum conductance was set to 0.001 nS/cm^2, the maximum value for the Ca_HVA maximum conductance was set to 1e-05 nS/cm^2, and the minimum value of the Im maximum conductance was set to 0.0002 nS/cm^2. These values were determined after rigorous investigation of the effects of these maximum conductances on the spiking properties.

Further constraints were placed on the passive properties of the neuron to make sure the neuron not only matched "charging" and "discharging" properties in the current clamp data, but also reasonably approximated the resistance and membrane time constant values from the experimental

data (***Chameh et al., 2019***). These limits were as follows: the axial resistance (Ra) was constrained between 0 and 1000 ohm cm; the membrane capacitance (cm) outside the soma was constrained between 1 and 1.8 uF/cm^2; the passive reversal potential (e_pas) was constrained between -90 and -80 mV; and the passive conductance (g_pas) was constrained between 1.75e-05 and 2.5e-05 nS/cm^2.

In silico experiments

The usefulness of the model presented here lies not only in its ability to well "fit" the constraining data, but the insights it provides when subjected to *in silico* versions of experiments. Two common protocols used to assess sub- and suprathreshold neural activity were performed *in silico* on our model neuron to evaluate the ability of our neuron model to capture an "essence" of the functional capacity of the neuron, and this data was compared to available results from analogous *in vitro* experiments.

ZAP function

A "ZAP function", a sinusoidal function whose frequency changes linearly over a given range, has been used to assess the impedance amplitude profile in a variety of engineering settings for over 30 years (***Puil et al., 1986***), including in the assessment of subthreshold resonance properties in neurons (***Leung and Yu, 1998***). In this study, the ZAP function protocol was motivated by that used in the corresponding experimental data (***Chameh et al., 2019***): the current injection lasted for 20 seconds with its frequency ranging from 0 to 20 Hz. The current was injected into the soma of the model, just as the experimental protocol was somatic. The amplitude of this input was 0.03 pA in all *in silico* protocols.

We note that, in Figure 7**A**, only a single experiment is shown. As the ZAP current is set and the model neuron is deterministic (i.e. will exhibit the same response to the same input in every case), no averaging or statistical measures were necessary for this protocol.

We also note that, in determining the "resonant frequency" highlighted in Tables 2, 3, and 4, we only consider frequencies greater than 1 Hz, as a peak below 1 Hz can arise in these computational experiments as an artifact potentially driven by initial conditions, but does not indicate a biologically interesting frequency preference of the neuron. The peak values displayed in these tables were found simply by determining the frequency corresponding to the maximum impedance value (in the raw, rather than "smoothed", data).

The code generating this current was obtained from the NEURON (***Carnevale and Hines, 2006***) website via the following link: http://www.neuron.yale.edu/ftp/ted/neuron/izap.zip.

Frequency-dependent gain calculated via injection of Gaussian-filtered white noise

To evaluate whether the suprathreshold dynamics of the model neuron matched experimental findings, we evaluated the frequency-dependent gain of the model by injecting Gaussian-filtered white noise, with varying DC current shifts, to the soma. This technique is described above in relation to the experimental calculation of this feature (***Higgs and Spain, 2009***) .

In this implementation, the noise had a 40 pA gain, a tau value of 3 ms, and DC shifts were chosen so that the firing rate of the neuron fell within the general theta range (here, 4-10 Hz). The "noise" was generated via an in-house Matlab file, then imported into NEURON via the tools associated with the "vector" data type. The DC shift was added to the noise within the NEURON code, and then this current profile was injected into the soma of the model neuron (to match the somatic experiments of ***Chameh et al.*** (***2019***)). The voltage of the model neuron over time was outputted and then processed to generate an impedance plot utilizing additional in-house Matlab code implementing the measure presented in ***Higgs and Spain*** (***2009***) (described in detail above).

The plots presented in Figure 11**A** utilize a log-scale on the x-axis, again to match what is seen in analogous *in vitro* experiments. Figure 11**Ai-ii** are examples from a single trial, while Figure 11**Aiii** is an average over 60 trials with independently generated noisy components of the current. The gain

profiles were generated via in-house Matlab scripts that are included at https://github.com/FKSkinnerLab/HumanL5NeuronModel.

Implementation of other models

Models from two other works, that of ***Hay et al.*** (***2011***) and ***Kalmbach et al.*** (***2018***), were implemented and used for comparison purposes.

The ***Hay et al.*** (***2011***) model is accessible via ModelDB at senselab.med.yale.edu/ModelDB (Accession:139653). We implemented this model directly using the code available via this source. In this work we utilized the model that is "constrained both for BAC firing and Current Step Firing", which is dictated by specifically utilizing the "L5PCbiophys3.hoc" file.

The ***Kalmbach et al.*** (***2018***) model is available via GitHub at https://github.com/AllenInstitute/human_neuron_Ih. The morphology of the model neuron and the "shifted" version of the ***Kole et al.*** (***2006***) h-current model that are used were directly downloaded from this repository, and the passive properties and h-current maximum conductance values as defined in the code repository were instantiated via basic NEURON code. This "shifted" version of the ***Kole et al.*** (***2006***) model is included below:

$$
\begin{aligned}
i_{hcn} &= \text{glh} * (v - ehcn) \\
\text{glh} &= \text{glhbar} * m \\
\frac{dm}{dt} &= (m_\infty - m)/m_\tau \\
m_\alpha &= 0.001 * 6.43 * (v - 20 + 154.3)/(\exp((v - 20 + 154.9/11.9) - 1) \\
m_\beta &= 0.001 * 193 * \exp(v/33.1) \\
m_\infty &= \frac{m_\alpha}{m_\alpha + m_\beta} \\
m_\tau &= \frac{1}{m_\alpha + m_\beta}
\end{aligned}
\tag{7}
$$

The "-20" term in the m_α equation is the "shift" from ***Kole et al.*** (***2006***). The parameters dictating the model which has non-uniform passive properties and uniformly distributed h-channels (amongst the soma, apical, and basilar dendrites) are given in Table 7. We ensured our implementation of this model was appropriate by directly replicating Figure 7B of ***Kalmbach et al.*** (***2018***) with this implementation.

In both cases, replacing the default rodent-motivated h-current model with the h-current model generated in this study was a straightforward matter of changing which channel was added into the NEURON model. Doing so ensured that the *only* change in these "hybrid" models was to the kinetics of the h-current (i.e the h-channel distribution and maximum conductance, as well as all other features, were the same as in the "model backbone"). All code involved in the implementations of these models is available at https://github.com/FKSkinnerLab/HumanL5NeuronModel.

Table 7. Parameters used in implementation of the human L3 cortical pyramidal cell model of ***Kalmbach et al.*** (***2018***).

Parameter	Value
gIh, nS/cm^2	0.0001
Ra (soma), ohm cm	304.425
Ra (apical), ohm cm	393.534
Ra (basilar), ohm cm	104.085
Ra (axonal), ohm cm	331.682
cm (soma), uF/cm^2	2.72372
cm (apical), uF/cm^2	2.91188
cm (basilar), uF/cm^2	1.81391
cm (axonal), uF/cm^2	1.75213
g_pas (soma) nS/cm^2	1.90172e-05
g_pas (apical) nS/cm^2	3.02942-04
g_pas (basilar) nS/cm^2	4.46002e-06
g_pas (axonal) nS/cm^2	4.79653e-04
e_pas (soma), mV	-79.6515
e_pas (apical), mV	-84.5477
e_pas (basilar), mV	-86.6748
e_pas (axonal), mV	-65.3528

Acknowledgments

We thank Happy Inibhunu for applying new data visualization techniques to this model that helped to shape the presentation of these results.

References

Akam T, Kullmann DM. Oscillatory multiplexing of population codes for selective communication in the mammalian brain. Nature Reviews Neuroscience. 2014; 15(2):111–122. doi: 10.1038/nrn3668.

Almog M, Korngreen A. A quantitative description of dendritic conductances and its application to dendritic excitation in layer 5 pyramidal neurons. Journal of Neuroscience. 2014; 34(1):182–196. doi: 10.1523/JNEUROSCI.2896-13.2014.

Almog M, Korngreen A. Is realistic neuronal modeling realistic? Journal of neurophysiology. 2016; 116(5):2180–2209. doi: 10.1152/jn.00360.2016.

Anastassiou CA, Perin R, Markram H, Koch C. Ephaptic coupling of cortical neurons. Nature neuroscience. 2011; 14(2):217. doi: 10.1038/nn.2727.

Ascoli GA, Gasparini S, Medinilla V, Migliore M. Local control of postinhibitory rebound spiking in CA1 pyramidal neuron dendrites. Journal of Neuroscience. 2010; 30(18):6434–6442. doi: 10.1523/JNEUROSCI.4066-09.2010.

Beaulieu-Laroche L, Toloza EH, van der Goes MS, Lafourcade M, Barnagian D, Williams ZM, Eskandar EN, Frosch MP, Cash SS, Harnett MT. Enhanced dendritic compartmentalization in human cortical neurons. Cell. 2018; 175(3):643–651. doi: 10.1016/j.cell.2018.08.045.

Bianchi D, Marasco A, Limongiello A, Marchetti C, Marie H, Tirozzi B, Migliore M. On the mechanisms underlying the depolarization block in the spiking dynamics of CA1 pyramidal neurons. Journal of computational neuroscience. 2012; 33(2):207–225. doi: 10.1007/s10827-012-0383-y.

Biel M, Wahl-Schott C, Michalakis S, Zong X. Hyperpolarization-Activated Cation Channels: From Genes to Function. Physiological Reviews. 2009 Jul; 89(3):847–885. doi: 10.1152/physrev.00029.2008.

Brent R. A new algorithm for minimizing a function of several variables without calculating derivatives. Algorithms for minimization without derivatives. 1976; p. 200–248.

1069 **Carnevale NT**, Hines ML. The NEURON book. Cambridge University Press; 2006.

1070 **Chameh HM**, Wang L, Rich S, Zhang L, Carlen PL, Tripathy SJ, Valiante TA. Sag currents are a major contributor
1071 to human pyramidal cell intrinsic differences across cortical layers and between individuals. bioRxiv. 2019; p.
1072 748988. doi: 10.1101/748988.

1073 **Chen S**, Wang J, Siegelbaum SA. Properties of hyperpolarization-activated pacemaker current defined by
1074 coassembly of HCN1 and HCN2 subunits and basal modulation by cyclic nucleotide. The Journal of general
1075 physiology. 2001; 117(5):491–504. doi: 10.1085/jgp.117.5.491.

1076 **Dembrow NC**, Chitwood RA, Johnston D. Projection-specific neuromodulation of medial prefrontal cortex
1077 neurons. Journal of Neuroscience. 2010; 30(50):16922–16937. doi: 10.1523/JNEUROSCI.3644-10.2010.

1078 **Dong HW**. The Allen reference atlas: A digital color brain atlas of the C57Bl/6J male mouse. John Wiley & Sons
1079 Inc; 2008.

1080 **Dyhrfjeld-Johnsen J**, Morgan RJ, Soltesz I. Double trouble? Potential for hyperexcitability following both
1081 channelopathic up-and downregulation of Ih in epilepsy. Frontiers in neuroscience. 2009; 3:5. doi:
1082 10.3389/neuro.01.005.2009.

1083 **Einevoll GT**, Destexhe A, Diesmann M, Grün S, Jirsa V, Kamps Md, Migliore M, Ness TV, Plesser HE,
1084 Schürmann F. The Scientific Case for Brain Simulations. Neuron. 2019 May; 102(4):735–744. doi:
1085 10.1016/j.neuron.2019.03.027.

1086 **Eyal G**, Verhoog MB, Testa-Silva G, Deitcher Y, Benavides-Piccione R, DeFelipe J, De Kock CP, Mansvelder H, Segev
1087 I. Human cortical pyramidal neurons: From spines to spikes via models. Frontiers in cellular neuroscience.
1088 2018; 12:181. doi: 10.3389/fncel.2018.00181.

1089 **Eyal G**, Verhoog MB, Testa-Silva G, Deitcher Y, Lodder JC, Benavides-Piccione R, Morales J, DeFelipe J, de Kock CP,
1090 Mansvelder HD, et al. Unique membrane properties and enhanced signal processing in human neocortical
1091 neurons. Elife. 2016; 5:e16553. doi: 10.7554/eLife.16553.

1092 **Farinella M**, Ruedt DT, Gleeson P, Lanore F, Silver RA. Glutamate-bound NMDARs arising from in vivo-like
1093 network activity extend spatio-temporal integration in a L5 cortical pyramidal cell model. PLoS computational
1094 biology. 2014; 10(4):e1003590. doi: 10.1371/journal.pcbi.1003590.

1095 **Florez CM**, McGinn RJ, Lukankin V, Marwa I, Sugumar S, Dian J, Hazrati LN, Carlen PL, Zhang L, Valiante TA. In
1096 Vitro Recordings of Human Neocortical Oscillations. Cerebral Cortex. 2013 Sep; p. bht235. doi: 10.1093/cer-
1097 cor/bht235.

1098 **Fries P**. A mechanism for cognitive dynamics: neuronal communication through neuronal coherence. Trends in
1099 cognitive sciences. 2005; 9(10):474–480. doi: 10.1016/j.tics.2005.08.011.

1100 **Galán RF**, Ermentrout GB, Urban NN. Optimal time scale for spike-time reliability: theory, simulations, and
1101 experiments. Journal of neurophysiology. 2008; 99(1):277–283. doi: 10.1152/jn.00563.2007.

1102 **Goaillard JM**, Taylor AL, Schulz DJ, Marder E. Functional consequences of animal-to-animal variation in circuit
1103 parameters. Nature neuroscience. 2009; 12(11):1424. doi: 10.1038/nn.2404.

1104 **Golowasch J**, Goldman MS, Abbott L, Marder E. Failure of averaging in the construction of a conductance-based
1105 neuron model. Journal of Neurophysiology. 2002; 87(2):1129–1131. doi: 10.1152/jn.00412.2001.

1106 **Gouwens NW**, Berg J, Feng D, Sorensen SA, Zeng H, Hawrylycz MJ, Koch C, Arkhipov A. Systematic generation of
1107 biophysically detailed models for diverse cortical neuron types. Nature communications. 2018; 9(1):710. doi:
1108 10.1038/s41467-017-02718-3.

1109 **Hanslmayr S**, Axmacher N, Inman CS. Modulating Human Memory via Entrainment of Brain Oscillations. Trends
1110 in Neurosciences. 2019 Jul; 42(7):485–499. doi: 10.1016/j.tins.2019.04.004.

1111 **Harnett MT**, Magee JC, Williams SR. Distribution and function of HCN channels in the apical dendritic tuft of neo-
1112 cortical pyramidal neurons. Journal of Neuroscience. 2015; 35(3):1024–1037. doi: 10.1523/JNEUROSCI.2813-
1113 14.2015.

1114 **Hay E**, Hill S, Schürmann F, Markram H, Segev I. Models of neocortical layer 5b pyramidal cells capturing a wide
1115 range of dendritic and perisomatic active properties. PLoS computational biology. 2011; 7(7):e1002107. doi:
1116 10.1371/journal.pcbi.1002107.

1117 **Higgs MH**, Spain WJ. Conditional bursting enhances resonant firing in neocortical layer 2–3 pyramidal neurons.
1118 Journal of Neuroscience. 2009; 29(5):1285–1299. doi: 10.1523/JNEUROSCI.3728-08.2009.

1119 **Hines ML**, Carnevale NT. NEURON: a tool for neuroscientists. The neuroscientist. 2001; 7(2):123–135. doi:
1120 10.1177/107385840100700207.

1121 **Hodge RD**, Bakken TE, Miller JA, Smith KA, Barkan ER, Graybuck LT, Close JL, Long B, Johansen N, Penn O, Yao
1122 Z, Eggermont J, Höllt T, Levi BP, Shehata SI, Aevermann B, Beller A, Bertagnolli D, Brouner K, Casper T, et al.
1123 Conserved cell types with divergent features in human versus mouse cortex. Nature. 2019 Aug; p. 1–8. doi:
1124 10.1038/s41586-019-1506-7.

1125 **Hu H**, Vervaeke K, Graham LJ, Storm JF. Complementary Theta Resonance Filtering by Two Spatially Segregated
1126 Mechanisms in CA1 Hippocampal Pyramidal Neurons. The Journal of Neuroscience. 2009 Nov; 29(46):14472–
1127 14483. doi: 10.1523/JNEUROSCI.0187-09.2009.

1128 **Hu H**, Vervaeke K, Storm JF. Two forms of electrical resonance at theta frequencies, generated by M-current,
1129 h-current and persistent Na+ current in rat hippocampal pyramidal cells. The Journal of physiology. 2002;
1130 545(3):783–805. doi: 10.1113/jphysiol.2002.029249.

1131 **Hutcheon B**, Miura RM, Puil E. Subthreshold membrane resonance in neocortical neurons. Journal of neuro-
1132 physiology. 1996; 76(2):683–697. doi: 10.1152/jn.1996.76.2.683.

1133 **Hutcheon B**, Yarom Y. Resonance, oscillation and the intrinsic frequency preferences of neurons. Trends in
1134 Neurosciences. 2000 May; 23(5):216–222. doi: 10.1016/S0166-2236(00)01547-2.

1135 **Jones AR**, Overly CC, Sunkin SM. The Allen brain atlas: 5 years and beyond. Nature Reviews Neuroscience. 2009;
1136 10(11):821. doi: 10.1038/nrn2722.

1137 **Kalmbach BE**, Buchin A, Long B, Close J, Nandi A, Miller JA, Bakken TE, Hodge RD, Chong P, de Frates R, et al.
1138 h-Channels Contribute to Divergent Intrinsic Membrane Properties of Supragranular Pyramidal Neurons in
1139 Human versus Mouse Cerebral Cortex. Neuron. 2018; 100(5):1194–1208. doi: 10.1016/j.neuron.2018.10.012.

1140 **Keren N**, Bar-Yehuda D, Korngreen A. Experimentally guided modelling of dendritic excitability in rat neocortical
1141 pyramidal neurones. The Journal of physiology. 2009; 587(7):1413–1437. doi: 10.1113/jphysiol.2008.167130.

1142 **Kispersky TJ**, Fernandez FR, Economo MN, White JA. Spike resonance properties in hippocampal O-LM
1143 cells are dependent on refractory dynamics. Journal of Neuroscience. 2012; 32(11):3637–3651. doi:
1144 10.1523/JNEUROSCI.1361-11.2012.

1145 **Köhling R**, Avoli M. Methodological approaches to exploring epileptic disorders in the human brain in vitro.
1146 Journal of neuroscience methods. 2006; 155(1):1–19. doi: 10.1016/j.jneumeth.2006.04.009.

1147 **Kole MH**, Hallermann S, Stuart GJ. Single Ih channels in pyramidal neuron dendrites: properties, distri-
1148 bution, and impact on action potential output. Journal of Neuroscience. 2006; 26(6):1677–1687. doi:
1149 10.1523/JNEUROSCI.3664-05.2006.

1150 **Kostopoulos G**, Drapeau C, Avoli M, Olivier A, Villemeure JG. Endogenous adenosine can reduce epileptiform
1151 activity in the human epileptogenic cortex maintained in vitro. Neuroscience letters. 1989; 106(1-2):119–124.
1152 doi: 10.1016/0304-3940(89)90212-7.

1153 **Larkum ME**, Nevian T, Sandler M, Polsky A, Schiller J. Synaptic integration in tuft dendrites of layer 5 pyramidal
1154 neurons: a new unifying principle. Science. 2009; 325(5941):756–760. doi: 10.1126/science.1171958.

1155 **Larkum ME**, Zhu JJ. Signaling of layer 1 and whisker-evoked Ca2+ and Na+ action potentials in distal and
1156 terminal dendrites of rat neocortical pyramidal neurons in vitro and in vivo. Journal of neuroscience. 2002;
1157 22(16):6991–7005. doi: 10.1523/JNEUROSCI.22-16-06991.2002.

1158 **Larkum ME**, Zhu JJ, Sakmann B. A new cellular mechanism for coupling inputs arriving at different cortical
1159 layers. Nature. 1999; 398(6725):338. doi: doi.org/10.1038/18686.

1160 **Leung LS**, Yu HW. Theta-frequency resonance in hippocampal CA1 neurons in vitro demonstrated by sinusoidal
1161 current injection. Journal of neurophysiology. 1998; 79(3):1592–1596. doi: 10.1152/jn.1998.79.3.1592.

1162 **Mansouri A**, Fallah A, Valiante TA. Determining surgical candidacy in temporal lobe epilepsy. Epilepsy research
1163 and treatment. 2012; 2012. doi: 10.1155/2012/706917.

Marder E, Goaillard JM. Variability, compensation and homeostasis in neuron and network function. Nature Reviews Neuroscience. 2006; 7(7):563. doi: 10.1038/nrn1949.

MATLAB. version 9.6.0 (R2019a). Natick, Massachusetts: The MathWorks Inc.; 2019.

McGinn RJ, Valiante TA. Phase–Amplitude Coupling and Interlaminar Synchrony Are Correlated in Human Neocortex. The Journal of Neuroscience. 2014 Nov; 34(48):15923–15930. doi: 10.1523/JNEUROSCI.2771-14.2014.

Mohan H, Verhoog MB, Doreswamy KK, Eyal G, Aardse R, Lodder BN, Goriounova NA, Asamoah B, B Brakspear AC, Groot C, et al. Dendritic and axonal architecture of individual pyramidal neurons across layers of adult human neocortex. Cerebral Cortex. 2015; 25(12):4839–4853. doi: 10.1093/cercor/bhv188.

Molnár G, Oláh S, Komlósi G, Füle M, Szabadics J, Varga C, Barzó P, Tamás G. Complex events initiated by individual spikes in the human cerebral cortex. PLoS biology. 2008; 6(9):e222. doi: 10.1371/journal.pbio.0060222.

Neske GT, Connors BW. Distinct roles of SOM and VIP interneurons during cortical up states. Frontiers in Neural Circuits. 2016; 10:52. doi: 10.3389/fncir.2016.00052.

Neske GT, Connors BW. Synchronized gamma-frequency inhibition in neocortex depends on excitatory-inhibitory interactions but not electrical synapses. Journal of neurophysiology. 2016; 116(2):351–368. doi: 10.1152/jn.00071.2016.

Puil E, Gimbarzevsky B, Miura R. Quantification of membrane properties of trigeminal root ganglion neurons in guinea pigs. Journal of Neurophysiology. 1986; 55(5):995–1016. doi: 10.1152/jn.1986.55.5.995.

Ramaswamy S, Markram H. Anatomy and physiology of the thick-tufted layer 5 pyramidal neuron. Frontiers in cellular neuroscience. 2015; 9:233. doi: 10.3389/fncel.2015.00233.

Ransdell JL, Nair SS, Schulz DJ. Neurons within the same network independently achieve conserved output by differentially balancing variable conductance magnitudes. Journal of Neuroscience. 2013; 33(24):9950–9956. doi: 10.1523/JNEUROSCI.1095-13.2013.

Roth A, Bahl A. Divide et impera: optimizing compartmental models of neurons step by step. The Journal of physiology. 2009; 587(7):1369–1370. doi: 10.1113/jphysiol.2009.170944.

Rotstein HG. Spiking resonances in models with the same slow resonant and fast amplifying currents but different subthreshold dynamic properties. Journal of Computational Neuroscience. 2017 Dec; 43(3):243–271. doi: 10.1007/s10827-017-0661-9.

Rotstein HG, Nadim F. Frequency preference in two-dimensional neural models: a linear analysis of the interaction between resonant and amplifying currents. Journal of Computational Neuroscience. 2014 Aug; 37(1):9–28. doi: 10.1007/s10827-013-0483-3.

Schmidt SL, Dorsett CR, Iyengar AK, Fröhlich F. Interaction of intrinsic and synaptic currents mediate network resonance driven by layer V pyramidal cells. Cerebral Cortex. 2016; 27(9):4396–4410. doi: 10.1093/cercor/bhw242.

Sekulić V, Yi F, Garrett T, Guet-McCreight A, Lopez YY, Solis-Wheeler M, Wang R, Liu X, Lawrence JJ, Skinner FK. Somatodendritic HCN channels in hippocampal OLM cells revealed by a convergence of computational models and experiments. BioRxiv. 2019; p. 633941. doi: 10.1101/633941.

Sekulić V, Skinner FK. Computational models of O-LM cells are recruited by low or high theta frequency inputs depending on h-channel distributions. eLife. 2017 Mar; 6:e22962. doi: 10.7554/eLife.22962.

Shah MM. Neuronal HCN channel function and plasticity. Current Opinion in Physiology. 2018; 2:92–97. doi: 10.1016/j.cophys.2018.01.001.

Shai AS, Anastassiou CA, Larkum ME, Koch C. Physiology of layer 5 pyramidal neurons in mouse primary visual cortex: coincidence detection through bursting. PLoS computational biology. 2015; 11(3):e1004090. doi: 10.1371/journal.pcbi.1004090.

Silva LR, Amitai Y, Connors BW. Intrinsic oscillations of neocortex generated by layer 5 pyramidal neurons. Science. 1991; 251(4992):432–435. doi: 10.1126/science.1824881.

Stark E, Eichler R, Roux L, Fujisawa S, Rotstein HG, Buzsáki G. Inhibition-induced theta resonance in cortical circuits. Neuron. 2013; 80(5):1263–1276. doi: 10.1016/j.neuron.2013.09.033.

Sun H, An S, Luhmann HJ, Kilb W. Resonance properties of GABAergic interneurons in immature GAD67-GFP mouse neocortex. Brain research. 2014; 1548:1–11. doi: 10.1016/j.brainres.2013.12.032.

Sunkin SM, Ng L, Lau C, Dolbeare T, Gilbert TL, Thompson CL, Hawrylycz M, Dang C. Allen Brain Atlas: an integrated spatio-temporal portal for exploring the central nervous system. Nucleic acids research. 2012; 41(D1):D996–D1008. doi: 10.1093/nar/gks1042.

Testa-Silva G, Verhoog MB, Linaro D, de Kock CPJ, Baayen JC, Meredith RM, De Zeeuw CI, Giugliano M, Mansvelder HD. High Bandwidth Synaptic Communication and Frequency Tracking in Human Neocortex. PLoS Biol. 2014 Nov; 12(11):e1002007. doi: 10.1371/journal.pbio.1002007.

Ting JT, Daigle TL, Chen Q, Feng G. Acute brain slice methods for adult and aging animals: application of targeted patch clamp analysis and optogenetics. In: *Patch-Clamp Methods and Protocols* Springer; 2014.p. 221–242. doi: 10.1007/978-1-4939-1096-0_14.

Toledo-Rodriguez M, Blumenfeld B, Wu C, Luo J, Attali B, Goodman P, Markram H. Correlation maps allow neuronal electrical properties to be predicted from single-cell gene expression profiles in rat neocortex. Cerebral Cortex. 2004; 14(12):1310–1327. doi: 10.1093/cercor/bhh092.

Ulrich D. Dendritic resonance in rat neocortical pyramidal cells. Journal of neurophysiology. 2002; 87(6):2753–2759. doi: 10.1152/jn.2002.87.6.2753.

Vaidya SP, Johnston D. Temporal synchrony and gamma-to-theta power conversion in the dendrites of CA1 pyramidal neurons. Nature Neuroscience. 2013 Dec; 16(12):1812–1820. doi: 10.1038/nn.3562.

Vaz AP, Inati SK, Brunel N, Zaghloul KA. Coupled ripple oscillations between the medial temporal lobe and neocortex retrieve human memory. Science. 2019 Mar; 363(6430):975–978. doi: 10.1126/science.aau8956.

Verhoog MB, Goriounova NA, Obermayer J, Stroeder J, Hjorth JJJ, Testa-Silva G, Baayen JC, Kock CPJd, Meredith RM, Mansvelder HD. Mechanisms Underlying the Rules for Associative Plasticity at Adult Human Neocortical Synapses. The Journal of Neuroscience. 2013 Oct; 33(43):17197–17208. doi: 10.1523/JNEUROSCI.3158-13.2013.

Wilson RI. It takes all kinds to make a brain. Nature Neuroscience. 2010 Oct; 13(10):1158–1160. doi: 10.1038/nn1010-1158.

Womelsdorf T, Valiante TA, Sahin NT, Miller KJ, Tiesinga P. Dynamic circuit motifs underlying rhythmic gain control, gating and integration. Nature neuroscience. 2014; 17(8):1031. doi: 10.1038/nn.3764.

Zemankovics R, Káli S, Paulsen O, Freund TF, Hájos N. Differences in subthreshold resonance of hippocampal pyramidal cells and interneurons: the role of h-current and passive membrane characteristics. The Journal of physiology. 2010; 588(12):2109–2132. doi: 10.1113/jphysiol.2009.185975.